

Impact of Massive Binary Star and Cosmic Evolution on Gravitational Wave Observations II: Double Compact Object Rates and Properties

Floor S. Broekgaarden,^{1*} Edo Berger,¹ Simon Stevenson,^{2,3} Stephen Justham,^{4,5,6,7} Ilya Mandel,^{8,3,9} Martyna Chruślińska,^{7,10} Lieke A. C. van Son,^{1,6,7} Tom Wagg,^{11,1,7} Alejandro Vigna-Gómez,^{12,13} Selma E. de Mink,^{7,6,1} Debatri Chattopadhyay,^{2,3} Coenraad J. Neijssel⁹

¹Center for Astrophysics | Harvard & Smithsonian, 60 Garden St., Cambridge, MA 02138, USA

²Center for Astrophysics and Supercomputing, Swinburne University of Technology, Hawthorn VIC 3122, Australia

³The ARC Center of Excellence for Gravitational Wave Discovery – OzGrav, Hawthorn VIC 3122, Australia

⁴School of Astronomy & Space Science, University of the Chinese Academy of Sciences, Beijing 100012, China

⁵National Astronomical Observatories, Chinese Academy of Sciences, Beijing 100012, China

⁶Anton Pannekoek Institute for Astronomy and GRAPPA, University of Amsterdam, Postbus 94249, 1090 GE Amsterdam, The Netherlands

⁷Max-Planck-Institut für Astrophysik, Karl-Schwarzschild-Straße 1, 85741 Garching, Germany

⁸Monash Centre for Astrophysics, School of Physics and Astronomy, Monash University, Clayton, Victoria 3800, Australia

⁹Birmingham Institute for Gravitational Wave Astronomy and School of Physics and Astronomy, University of Birmingham, Birmingham, B15 2TT, United Kingdom

¹⁰Institute of Mathematics, Astrophysics and Particle Physics, Radboud University Nijmegen, PO Box 9010, 6500 GL Nijmegen

¹¹Department of Astronomy, University of Washington, Seattle, WA, 98195

¹²Niels Bohr International Academy, The Niels Bohr Institute, Blegdamsvej 17, DK-2100 Copenhagen, Denmark

¹³DARK, Niels Bohr Institute, University of Copenhagen, Jagtvej 128, DK-2200, Copenhagen, Denmark

Accepted XXX. Received YYY; in original form ZZZ

ABSTRACT

Making the most of the rapidly increasing population of gravitational-wave detections of black hole (BH) and neutron star (NS) mergers requires comparing observations with population synthesis predictions. In this work we investigate the *combined* impact from the key uncertainties in population synthesis modelling of the isolated binary evolution channel: the physical processes in massive binary-star evolution and the star formation history as a function of metallicity, Z , and redshift z , $S(Z, z)$. Considering these uncertainties we create 560 different publicly available model realizations and calculate the rate and distribution characteristics of detectable BHBH, BHNS, and NSNS mergers. We find that our stellar evolution and $S(Z, z)$ variations can impact the predicted intrinsic and detectable merger rates by factors 10^2 – 10^4 . We find that BHBH rates are dominantly impacted by $S(Z, z)$ variations, NSNS rates by stellar evolution variations and BHNS rates by both. We then consider the combined impact from all uncertainties considered in this work on the detectable mass distribution shapes (chirp mass, individual masses and mass ratio). We find that the BHNS mass distributions are predominantly impacted by massive binary-star evolution changes. For BHBH and NSNS we find that both uncertainties are important. We also find that the shape of the delay time and birth metallicity distributions are typically dominated by the choice of $S(Z, z)$ for BHBH, BHNS and NSNS. We identify several examples of robust features in the mass distributions predicted by all 560 models, such that we expect more than 95 percent of BHBH detections to contain a BH $\gtrsim 8 M_{\odot}$ and have mass ratios $\lesssim 4$. Our work demonstrates that it is essential to consider a wide range of allowed models to study double compact object merger rates and properties. Conversely, larger observed samples could allow us to decipher currently unconstrained stages of stellar and binary evolution.

Key words: (transients:) black hole - neutron star mergers – gravitational waves – stars: evolution

1 INTRODUCTION

The population of detected gravitational-wave (GW) events from binary black hole (BHBH), black hole–neutron star (BHNS) and binary neutron star (NSNS) mergers is rapidly increasing (Abbott et al. 2019, 2020a, 2021a; The LIGO Scientific Collaboration et al. 2021b). These mergers carry unique information about the properties of BHs and NSs (such as their masses and spins), which in turn probes

the formation, lives, and explosive deaths of massive stars throughout cosmic history (e.g. Abbott et al. 2021b; The LIGO Scientific Collaboration et al. 2021c). To extract information from these double compact object (DCO) detections requires comparing their observed properties, to theoretically simulated populations modelling their formation pathways.

A variety of formation channels for DCO mergers have been proposed (see Mandel & Farmer 2018; Mapelli 2021, for reviews), with one of the most prominent pathways being the *isolated binary evolution channel*, where the merging DCO systems are assumed to form

* E-mail: floor.broekgaarden@cfa.harvard.edu

from pairs of massive stars in wide, isolated, binary systems. This formation pathway can currently account for the observed DCO rates (Mandel & Broekgaarden 2021) and many of the observed DCO source properties (e.g., Vigna-Gómez et al. 2018; Belczynski et al. 2020, Broekgaarden & Berger 2021, but see §4.2 for a discussion).

However, modelling theoretical populations of DCO mergers from the isolated binary evolution channel is challenging as the simulations suffer from two key uncertainties: First, various physical processes in massive binary star evolution are uncertain; these include key evolutionary stages such as wind mass loss, stable mass transfer, common envelope (CE) episodes, and supernovae (SNe), which significantly impact the predicted rates and properties of DCO mergers. Second, there are critical uncertainties in the cosmic star formation and chemical evolution history, which impact the metallicity-dependent star formation rate density $\mathcal{S}(Z, z)$, which is a function of birth metallicity Z and redshift z . Uncertainties in $\mathcal{S}(Z, z)$ also significantly impact the predicted rate and properties of DCO mergers as the birth metallicity significantly affects stellar evolution, including mass loss through line-driven winds and the (maximum) radial expansion.

Earlier works investigating the impact from stellar evolution and $\mathcal{S}(Z, z)$ uncertainties on the simulated DCO population typically focused on exploring only one of these two sets of uncertainties. For example, studies including Dominik et al. (2015), Giacobbo & Mapelli (2018), Kruckow et al. (2018), and Belczynski et al. (2020) explored population synthesis models with a large number of different massive binary stellar evolution assumptions, but only investigated one or a few $\mathcal{S}(Z, z)$ models. On the other hand, studies including Chruślińska et al. (2019), Neijssel et al. (2019), Tang et al. (2020), and Briel et al. (2021) focused on exploring a wide range of $\mathcal{S}(Z, z)$ models, but only considered one or a few different stellar evolution realizations. By only focusing on one of the two uncertainties it remains challenging to directly understand the combined or relative impact from the massive (binary) stellar evolution and $\mathcal{S}(Z, z)$ uncertainties on the detectable DCO population. This limits our ability to learn from GW observations and constrain the models.

Recently, Santoliquido et al. (2021) improved on this by presenting a large set of binary star evolution model variations (for mass transfer, CE phases and SNe) as well as $\mathcal{S}(Z, z)$ models, exploring the impact from each of the uncertainties on the predicted DCO merger rates (although the authors do not present the *combined* impact from both uncertainties except for their $\alpha 1$ and $\alpha 5$ model variations in their Figure 7). In addition, Chu et al. (2021) carried out a large study investigating the impact from variations in the CE phase and SN kicks in combination with four different $\mathcal{S}(Z, z)$ models focusing on their impact on the merger rates of NSNS mergers. However, besides impacting the merger rates, variations in stellar evolution models and $\mathcal{S}(Z, z)$ are also expected to impact the DCO merger *distribution shapes* of the properties of the detectable mergers. A large systematic study exploring this for GW events from all three types of DCO mergers (BHBH, BHNS and NSNS) is currently missing.

In Broekgaarden et al. (2021, from hereon Paper I), we improved on this by investigating the *combined* impact from uncertainties in both massive binary star evolution and the $\mathcal{S}(Z, z)$ on the predicted rate and *distribution shapes* focusing on, as a first step, the GW-detectable BHNS mergers. Here we continue this work by studying all three GW-detectable DCO merger types and by adding extra model realizations. We use rapid binary stellar evolution synthesis simulations coupled with analytical prescriptions for $\mathcal{S}(Z, z)$ to present the DCO rate and properties for a total of 560 model realizations. Our method is described in §2. We present the impact from the physical processes in massive binary star evolution and $\mathcal{S}(Z, z)$ on the predicted rate and shape of the distribution functions for DCO mergers

in §3. We discuss these results in §4 and present our conclusions in §5.

2 METHOD

We use the simulations and methodology presented in Paper I. Here we add new models F, G, J, S and T, which leads to a minor shift in the model labels. Our models explore the key assumptions in both massive (binary) star evolution and $\mathcal{S}(Z, z)$, leading to 560 (20 binary stellar evolution \times 28 $\mathcal{S}(Z, z)$) model realizations. We particularly choose our model variations to explore a broad span of uncertainty in the modelling. For that reason some of the variations are somewhat extreme (e.g., models S and T), but are chosen to explore their possible impact on the rate and distribution shapes of DCO mergers. We summarize our most important model assumptions below and summarize the model variations in Table 1 (massive binary star evolution) and Table A1 ($\mathcal{S}(Z, z)$). More details can be found in the Appendix and in Paper I.

2.1 Massive binary-star population models

We simulate populations of GW sources with the rapid binary population synthesis code from the COMPAS¹ suite (Stevenson et al. 2017; Barrett et al. 2018; Vigna-Gómez et al. 2018; Broekgaarden et al. 2019; Neijssel et al. 2019; Team COMPAS: J. Riley et al. 2021). We model the formation of BH and NS mergers from the *isolated binary evolution* channel where the merging DCOs form from massive stars born in a binary system (Smarr & Blandford 1976; Srinivasan 1989). We explore uncertainties in our massive (binary) star evolution assumptions by studying 20 binary population synthesis model variations. We further use the efficient sampling algorithm STROOPWAFEL (Broekgaarden et al. 2019) to simulate $\geq 10^6$ binary systems for 53 different Z values, resulting in typically $\sim 10^7$ DCO mergers in each simulation, making it one of the best-sampled population synthesis studies of its kind.

For our default model (A) settings we use the fiducial model summarized in Paper I. For the remaining models we change one population parameter at a time (relative to the fiducial model) to explore the impact of the uncertain model assumptions. The only exception is model F (E+K), which combines the model changes from both models E and K. Our 20 models are summarized in Table 1 and we refer to them throughout the rest of the paper by the letters A to T and the abbreviated label names given in the second column of Table 1. We focus on (and decide to use) the stellar evolution and the $\mathcal{S}(Z, z)$ variations mentioned below as these are commonly used in population synthesis settings, see Broekgaarden et al. (2021) for more details.

In models B, C, D, E and F we explore uncertainties in binary mass transfer prescriptions. Of these, models B, C and D vary the mass transfer efficiency. This is defined in COMPAS by the parameter β , which determines for a given donated mass rate the fraction that is accreted by the companion star: $\beta \equiv (dM_{\text{acc}}/dt)/(-dM_{\text{donor}}/dt)$, with M_{acc} and M_{donor} being the mass of the accretor and donor stars, respectively, and t the time (where dt is the simulation time step). The excess mass is assumed to leave the binary from the vicinity of the accreting star through ‘isotropic re-emission’ (e.g., Masetvitch & Yungelson 1975; Bhattacharya & van den Heuvel 1991;

¹ Compact Object Mergers: Population Astrophysics and Statistics, <https://compas.science>

μ	Label	Variation
A	fiducial	–
B	$\beta = 0.25$	fixed mass transfer efficiency of $\beta = 0.25$
C	$\beta = 0.5$	fixed mass transfer efficiency of $\beta = 0.5$
D	$\beta = 0.75$	fixed mass transfer efficiency of $\beta = 0.75$
E	unstable/no case BB	case BB mass transfer is always unstable
F	E + K	case BB mass transfer is always unstable & HG donor stars initiating a CE may survive
G	$\alpha = 0.1$	CE efficiency parameter $\alpha = 0.1$
H	$\alpha = 0.5$	CE efficiency parameter $\alpha = 0.5$
I	$\alpha = 2$	CE efficiency parameter $\alpha = 2$
J	$\alpha = 10$	CE efficiency parameter $\alpha = 10$
K	optimistic CE	HG donor stars initiating a CE may survive
L	rapid SN	Fryer rapid SN remnant mass model
M	$m_{\text{NS}} = 2 M_{\odot}$	maximum NS mass is fixed to $2 M_{\odot}$
N	$m_{\text{NS}} = 3 M_{\odot}$	maximum NS mass is fixed to $3 M_{\odot}$
O	no PISN	no PISN and pulsational-PISN
P	$\sigma_{\text{rms}}^{\text{1D}} = 100 \text{ km s}^{-1}$	$\sigma_{\text{rms}}^{\text{1D}} = 100 \text{ km s}^{-1}$ for core-collapse SNe
Q	$\sigma_{\text{rms}}^{\text{1D}} = 30 \text{ km s}^{-1}$	$\sigma_{\text{rms}}^{\text{1D}} = 30 \text{ km s}^{-1}$ for core-collapse SNe
R	$v_{\text{k,BH}} = 0$	we assume BHs receive no natal kick
S	$f_{\text{WR}} = 0.1$	Wolf-Rayet wind factor $f_{\text{WR}} = 0.1$
T	$f_{\text{WR}} = 5$	Wolf-Rayet wind factor $f_{\text{WR}} = 5$

Table 1. List of the 20 binary population synthesis models studied in this work. μ and ‘Label’ denote the alphabetical letter and abbreviated name used to label each model, ‘Variation’ denotes what we changed compared to the fiducial settings (model A). Models B, C, D, E and F vary mass transfer assumptions, models G, H, I, J and K vary common-envelope assumptions, models L, M, N, O, P, Q and R vary supernova assumptions and models S and T vary our Wolf-Rayet wind assumptions. Acronyms used are: common-envelope (CE), Hertzsprung Gap (HG), supernova (SN) neutron star (NS), black hole (BH) and pair-instability SN (PISN). We additionally use the subscripts root-mean-square (rms), one-dimensional (1D) and Wolf-Rayet (WR). Each model varies one assumption compared to the fiducial model, except for model F where we vary two assumptions (namely those from model E and K; unstable case BB and optimistic CE)

Soberman et al. 1997) and the angular momentum loss is calculated accordingly (cf., Equations 32 and 33 in Belczynski et al. 2008). Our fiducial model (A) assumes the accretion rate is limited by the star’s thermal timescale: $dM_{\text{acc}}/dt \leq 10M_{\text{acc}}/\tau_{\text{KH}}$, where τ_{KH} is the Kelvin-Helmholtz (thermal) timescale², and the factor of 10 is added to take into account the expansion of the accretor due to mass transfer (cf., Paczyński & Sienkiewicz 1972, Hurley et al. 2002 and Schneider et al. 2015). Models B, C and D assume a different accretion rate limit for stars by fixing β to 0.25, 0.5, and 0.75, respectively. All of our models assume an Eddington-limited accretion rate for compact objects. In our fiducial model we assume that case BB mass transfer, which is mass transfer from a stripped post-helium-burning star onto the accretor (Delgado & Thomas 1981), is always stable. Model E explores a variation where case BB (and case BC, but these are more rare) mass transfer is assumed to always be unstable, leading to a CE phase. This assumption causes case BB mass transferring systems to merge as stars in model E as our fiducial model assumes the now unstable CE phase initiated by a (helium) Hertzsprung Gap star is unsuccessful and leads to a merger (as described further in the ‘pes-

simistic CE assumption’ in the next paragraph). We therefore also add model F, which explores the effect of assuming unstable case BB mass transfer, but allowing Hertzsprung Gap donor stars to survive a CE phase (the ‘optimistic CE assumption’).

In models G, H, I, J and K we explore the effect of changing the CE prescription assumptions, which in COMPAS are parameterized using the ‘ α - λ ’ formalism from Webbink (1984) and de Kool (1990). Our fiducial model assumes a CE efficiency of $\alpha_{\text{CE}} = 1$ and uses for λ the ‘Nanjing lambda’ prescription (cf., Dominik et al. 2012), which is based on models from Xu & Li (2010a,b). In models G, H, I and J we change the CE efficiency to fixed values of 0.1, 0.5, 2 and 10, respectively. Compared to the fiducial model, lower and higher values of α_{CE} reduce and increase the efficiency with which the CE is ejected, respectively. In model K (and model F) we allow Hertzsprung gap stars that initiate a CE to possibly survive the CE (also known as the ‘optimistic’ CE assumption), whereas in our fiducial model these are assumed to always lead to an unsuccessful CE ejection (and merger), the ‘pessimistic’ CE scenario (cf., Dominik et al. 2012).

In models L, M, N, O, P, Q and R we vary the SN prescription assumptions. In model L we use the ‘rapid’ SN remnant mass model of Fryer et al. (2012) instead of their ‘delayed’ model, which is implemented in our fiducial model. The rapid model creates a mass gap between $\approx 2 - 6 M_{\odot}$, where no BHs form, whereas in the delayed model such BHs can form. Models M and N change our assumption for the maximum NS mass, by default $2.5 M_{\odot}$, to $2 M_{\odot}$ and $3 M_{\odot}$, respectively and we adapt the remnant mass prescription from Fryer et al. (2012) accordingly. In model O we do not use the prescription for pair-instability SNe and pulsational pair-instability SNe, therefore allowing the formation of BHs in the mass range of $\approx 40 - 100 M_{\odot}$. In models P and Q we change the root mean square velocity dispersion ($\sigma_{\text{rms}}^{\text{1D}}$) for the Maxwellian SN natal kick distribution for both BHs and NSs, to 100 km s^{-1} and 30 km s^{-1} , respectively (the fiducial model uses $\sigma_{\text{rms}}^{\text{1D}} = 265 \text{ km s}^{-1}$). For all our models we assume that a fraction of the ejected material (f_{fb}) falls back onto the compact object and we adjust the remnant mass and re-scale the SN kick magnitude accordingly (cf., Fryer et al. 2012). For ultra-stripped SNe and electron-capture SNe we always draw the SN kick using a one-dimensional root-mean-square velocity dispersion of $\sigma_{\text{rms}}^{\text{1D}} = 30 \text{ km s}^{-1}$ following Pfahl et al. (2002) and Podsiadlowski et al. (2004). In model R we assume instead that only all BHs receive zero natal kicks, $v_{\text{k}} = 0 \text{ km s}^{-1}$.

Finally, models S and T explore the assumptions for the mass loss rate in Wolf-Rayet winds. Our Wolf-Rayet wind prescription follows Belczynski et al. (2010), which is based on Hamann & Koesterke (1998) and Vink & de Koter (2005), by parameterizing the wind strength with a multiplicative parameter f_{WR} (cf., Barrett et al. 2018). By default we use $f_{\text{WR}} = 1$ and in models S and T we vary this to 0.1 and 5, respectively, which largely spans the possible range for Wolf-Rayet winds inferred from observations (e.g., Vink 2017; Hamann et al. 2019; Shenar et al. 2019; Sander & Vink 2020).

2.2 Metallicity-dependent star formation rate density models

The time between formation and merger of a DCO can range up to many Gyr (e.g., Neijssel et al. 2019). As a result, the DCOs that are detected by current ground-based GW observatories can originate from stars that formed throughout a wide range of redshifts with a large variety of birth metallicities (e.g., Chruslińska & Nelemans 2019). Similar to Paper I, we follow the method of Neijssel et al. (2019) to create a metallicity-dependent star formation rate density $S(Z, z)$, which describes the star formation history as a function of

² Given in Equation 61 of Hurley et al. (2002), where we use a pre-factor of 30 Myr from Equation 2 in Kalogera & Webbink (1996).

birth (initial) metallicity³ Z and redshift z . To explore uncertainties in $\mathcal{S}(Z, z)$, we use a total of 28 $\mathcal{S}(Z, z)$ models. Each model convolves a star formation rate density (SFRD)⁴ with a metallicity probability distribution function, dP/dZ . Our first model xyz = 000 (see Table A1 for the labeling) is the so-called ‘preferred’ phenomenological model from Neijssel et al. (2019), which they fit to match the BHBH observations from the first two observing runs by LIGO and Virgo. The other 27 ($3 \times 3 \times 3$) models are constructed by combining a SFRD with a galaxy stellar mass function, the number density of galaxies per logarithmic mass bin, (GSMF), and a mass-metallicity relation (MZR). The three variations for each SFRD, GSMF and MZR that we consider are given in Table A1. Although many of the prescriptions in these models oversimplify the complex $\mathcal{S}(Z, z)$ that is evident from observations, these prescriptions provide a convenient parametrization for binary population synthesis studies. For more details about caveats and uncertainties in the modelling of $\mathcal{S}(Z, z)$ within binary population synthesis we refer the reader to Chruślińska & Nelemans (2019), Neijssel et al. (2019), Boco et al. (2021) and references therein.

3 RESULTS

3.1 Metallicity specific merger yields

In Figure 1 we show the calculated formation yields ($\mathcal{R}_{\text{form}}$) for BHBH, BHNS and NSNS mergers per unit solar mass of stars formed (dM_{SFR}) as a function of Z for our 20 binary population synthesis models. This formation yield only includes DCO systems that have a GW driven inspiral time (t_{inspiral}) that is smaller than the Hubble time (≈ 14 Gyr) and is given by

$$\mathcal{R}_{\text{form}}(Z) = \frac{dN_{\text{form}}}{dM_{\text{SFR}}}(Z), \quad (1)$$

where we convert the number of mergers in our COMPAS realizations to formation yields by integrating our simulation range over the full initial parameter space of binary systems (e.g., the full initial mass range of stars) and assuming a corrected⁵ binary fraction of $f_{\text{bin}} = 1$ (consistent with e.g., Sana 2017). Details are given in Paper I.

3.1.1 Impact from the binary massive star evolution assumptions and metallicity

Figure 1 demonstrates that the variation in the BHBH merger formation yield is typically dominated by Z , causing variations on the order of $\mathcal{O}(10^2)$ between $Z \approx 0.001$ and $Z \approx Z_{\odot}$. Variations in our massive binary population synthesis assumptions impact the BHBH merger yield only with factors of up to ≈ 3 at $Z \lesssim 0.1 Z_{\odot}$ and on the order of $\mathcal{O}(10)$ for most stellar evolution models at higher Z . The exceptions to this include model T ($f_{\text{WR}} = 5$), which has a much lower BHBH yield (by $\mathcal{O}(10^2)$) compared to other stellar evolution models for $Z \gtrsim 0.2 Z_{\odot}$ where BH formation is drastically reduced due to the strong stellar wind mass loss. Other examples include

³ Where Z is the fractional metallicity, such that $X + Y + Z = 1$ with X and Y the mass fractions of hydrogen and helium, respectively.

⁴ We use $\mathcal{S}(Z, z)$ for the metallicity-dependent star formation rate density as a function of metallicity and redshift and SFRD for the total star formation rate density across all metallicities, which we model as only a function of redshift.

⁵ Corrected to take into account the differences in parameter range between population synthesis and observations, see de Mink & Belczynski (2015).

the optimistic CE models (F and K) that have higher BHBH yields compared to other stellar evolution models for $Z \gtrsim 0.2 Z_{\odot}$.

The scatter in the BHNS and NSNS formation yields, on the other hand, are typically dominated by variations in the stellar and binary evolution models over most of the Z range, leading to variations of $\gtrsim \mathcal{O}(10^2)$ in the rates, compared to typical ranges of $\lesssim \mathcal{O}(10)$ from variations in Z for most models.

3.1.2 Trends in the metallicity-dependent formation yields

As can be seen in Figure 1, the formation yield of BHBH mergers is constant at low metallicities and then steeply declines at $Z \gtrsim 0.1 Z_{\odot}$ for all model variations. This steep decline of merging BHBHs at higher metallicities has been pointed out previously (e.g., Belczynski et al. 2010; Dominik et al. 2012), and is consistent with various recent works including Giacobbo et al. (2018), Giacobbo & Mapelli (2018), Klencki et al. (2018), Chruślińska & Nelemans (2019), Neijssel et al. (2019) and Santoliquido et al. (2021), demonstrating that this trend is present among many different population synthesis studies and simulation settings. This decline is due to several metallicity dependent effects. First, stronger stellar winds at higher metallicities lead to increased mass loss and hence wider binaries with less massive DCOs, reducing the fraction of BHBHs that will merge in a Hubble time. In addition, the less massive BHs are assumed to have smaller amounts of fallback and hence receive larger natal kicks in our simulations, increasing the fraction that is disrupted during the SN (cf., Fryer et al. 2012; Klencki et al. 2018; Renzo et al. 2019). Indeed, in the model variations where BHs receive lower or no SN kick (Q and R) or the Wolf-Rayet winds are weaker (model S) the decline in BHBH yield is less severe in Figure 1. Second, there is a metallicity dependence of the radius expansion of stars in our single star evolution tracks (Hurley et al. 2000), leading more stars to enter the CE phase during the Hertzsprung Gap instead of during the giant phase at higher (\sim Solar) metallicities (cf., Figure 2 in Belczynski et al. 2010, Figure 7 in Linden et al. 2010 and Section 3.1.1 in Bavera et al. 2021). In our fiducial simulation such Hertzsprung Gap donor stars do not survive the CE phase. In models F (E+K) and K (optimistic CE) we instead assume these systems do survive, leading to a visible boost in BBH yields at higher Z , as seen in Figure 1.

The behavior of the BHNS yield in most models, on the other hand, first modestly increases as a function of Z and then declines around Z_{\odot} (Figure 1; cf., Klencki et al. 2018; Chruślińska & Nelemans 2019; Román-Garza et al. 2021). This causes the yield to broadly peak in the range $0.2 Z_{\odot} \lesssim Z \lesssim Z_{\odot}$, where the location of the peak varies between models as shown in Figure 1. The same metallicity dependent effects as described for BHBH mergers above are at play for BHNS mergers. However, since BHNS systems typically already form DCOs with lower mass BHs and form from lower mass stars compared to BHBH mergers, these BHNS systems do not experience the same boost in formation yields at low metallicities compared to the BHBH mergers, leading to lower yields at lower Z . In addition, the peak in BHNS yield is caused by the maximum radial extent of stars in the Hertzsprung Gap, which generally increases with Z but decreases between $10^{-3} \lesssim Z \lesssim 10^{-2}$ in our simulations for the zero-age main sequence mass range of BHNS progenitors (initial primary masses of $15 \lesssim m_{1,i}/M_{\odot} \lesssim 50$). This is based on the single star evolution prescriptions from Hurley et al. (2000) implemented in COMPAS. As a result of the smaller radii there are typically fewer stellar mergers in our simulations as fewer stars completely engulf their companion during mass transfer (as discussed by Giacobbo & Mapelli 2018) and the average initial separations of binaries that form merging BHNSs shifts to smaller values, which are more commonly

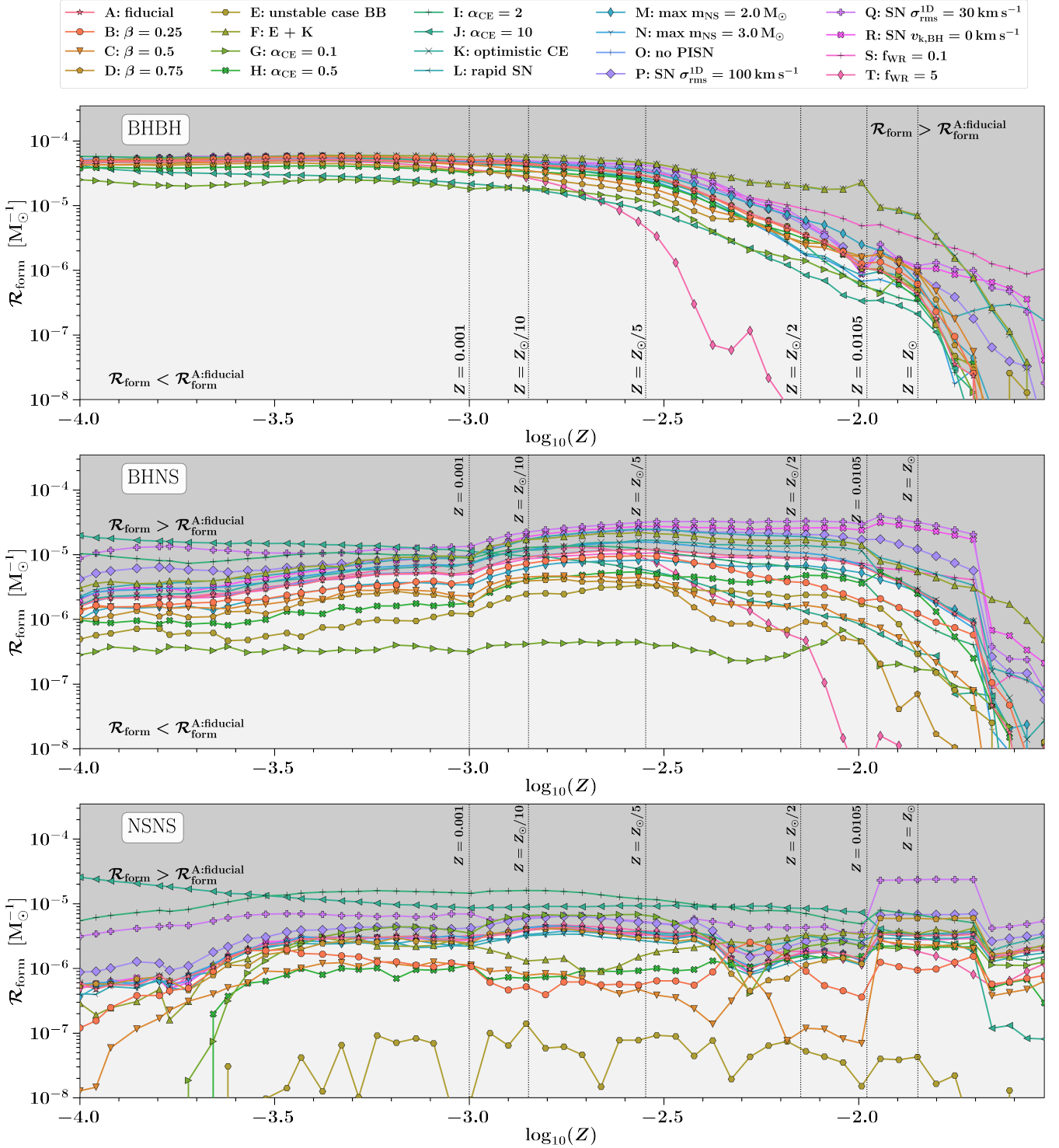


Figure 1. Formation yield of merging double compact objects per solar mass of star formation, $\mathcal{R}_{\text{form}} = dN_{\text{form}}/dM_{\text{SFR}}$ (Equation 1), as a function of birth metallicity Z . The yield only includes binaries that have GW-driven inspiral times ≤ 14 Gyr. From top to bottom the panels show the formation yields for merging BHBH, BHNS and NSNS, respectively. Each color and marker type correspond to one of the 20 binary population synthesis models explored in this study (Table 1). The dark and light gray areas in the background mark where the formation yield is larger and smaller compared to our fiducial model (A) yield. Vertical dotted lines show fixed Z values to guide the reader. The marker points show the Z grid values that we simulated with COMPAS in each simulation. The sharp increase in yield around $Z \approx 0.0105$, particularly visible in the NSNS panel, is caused by an artificial bifurcation in our λ values for the common-envelope treatment in COMPAS at this Z . The scatter in the unstable case BB mass transfer model (E) in the NSNS panel is caused by sampling noise. [b](#) [c](#)

formed. See also the discussion in §4.1.2 in [Klencki et al. \(2018\)](#) for additional details.

We find that the NSNS merger yield remains roughly constant as a function of Z (cf., [Chruślińska et al. 2018](#); [Klencki et al. 2018](#); [Giacobbo & Mapelli 2018](#); [Neijssel et al. 2019](#)) as the metallicity-dependent effects described above are less significant for lower-mass stars that form NSNS binaries. The strong increase in formation yield around $Z \approx 0.0105$ in Figure 1 that is particularly noticeable for NSNS binaries is due to a bifurcation in our λ prescription for the envelope binding energy (relevant for the CE phase) and is an artifact in our modelling. More orbital energy is needed to successfully unbind the envelope for $Z > 0.0105$ in our models. This means that the binary engulfed in the CE will need to move to tighter orbits in order to successfully eject the envelope. This results in tighter post-CE binaries that survive the second SN and can merge in a Hubble time, thereby increasing the rate. Finally, we note that the scatter in model E (unstable case BB) is caused by sampling noise as a consequence of the very small number of NSNS mergers (only 371) in this simulation⁶. In the next Section we discuss this model and show that it under-predicts the inferred NSNS rate from GW observations by two orders of magnitude.

Comparing the panels in Figure 1 we find that at low Z the formation yield of merging BHBHs in a Hubble time exceeds that of merging BHNSs and NSNSs. The merging BHNS formation yield starts dominating over the BHBH yield at $Z \gtrsim 0.3 Z_{\odot}$, whereas for merging NSNS this occurs at $Z \gtrsim 0.5 Z_{\odot}$ for most models. We show these merging DCO ratios in Figure A1. Using our $\mathcal{S}(Z, z)$ models we can translate these transition metallicities into approximate typical redshifts. For example, Figure A2 shows that the average metallicity of star formation is $\langle Z \rangle \approx 0.5 Z_{\odot}$ at $z \approx 3$ and $z \approx 0.4$ for the $xyz = 312$ and $xyz = 231$ $\mathcal{S}(Z, z)$ models, respectively. These two $\mathcal{S}(Z, z)$ models correspond to the highest and lowest average metallicity of star formation within our simulated $\mathcal{S}(Z, z)$ models and, as we will show in the next section, to one of the lowest and highest DCO merger rate density predictions, respectively.

3.2 Intrinsic merger rates

In Figure 2 we show the population synthesis calculated local (intrinsic) merger rate densities for BHBH, BHNS and NSNS binaries. There are three main findings that we describe in more detail below. First, we find that the combined variations in our massive binary star and $\mathcal{S}(Z, z)$ assumptions impact the intrinsic DCO rates with resulting ranges of ≈ 210 –1030. Second, only a subset of the 560 models matches the ranges for the inferred BHBH, BHNS and NSNS merger rate density from GW observations ([The LIGO Scientific Collaboration et al. 2021c](#)). Third, we find that the calculated merger rates for different types of DCO are sensitive to different uncertainties in the modelling. Most strikingly, we find that the BHBH merger rates are primarily sensitive to variations in $\mathcal{S}(Z, z)$ models, whereas the NSNS merger rates are predominantly impacted by binary stellar evolution model variations. This means that the observed BHBH and NSNS rates can provide a test-bed for $\mathcal{S}(Z, z)$ and stellar evolution uncertainties, respectively.

The intrinsic rates are calculated using the formation yields from Equation 1 and by taking into account the $\mathcal{S}(Z, z)$ weighting discussed in §2.2. The local merger rate is then obtained using $t_m(z \approx 0)$ in the equation (i.e. evaluating the equation at the center of our lowest

redshift bin for z)

$$\mathcal{R}_m(t_m) = \frac{d^2 N_{\text{merger}}}{dt_m dV_c}(t_m) = \int dZ \int_0^{t_m} dt_{\text{delay}} \mathcal{S}(Z, t_{\text{form}}) \frac{d^2 N_{\text{form}}}{dM_{\text{SFR}} dt_{\text{delay}}}(Z, t_{\text{delay}}), \quad (2)$$

where t_m again is time in the source frame measured from the Big Bang⁷, t_m is the time of the DCO merger, t_{delay} is the delay time between the formation of the DCO and its merger, and V_c is the co-moving volume. The delay time is $t_{\text{delay}} = t_{\text{evolve}} + t_{\text{inspiral}}$, the total time from the onset of hydrogen burning at ZAMS to forming a DCO, i.e., until the second SN (t_{evolve}), and the time it takes the DCO to coalesce from the moment of the second SN (t_{inspiral}); see Figure 1 in [Paper I](#) for more details. The binary initially forms at t_{form} , which we set as $t_{\text{form}} = t_m - t_{\text{delay}}$ in this equation. For the $\mathcal{S}(Z, z)$ we use the 28 models from Table A1. In practice we estimate Equation 2 with a Riemann sum where we sum over our metallicity grid and redshift (time) bins.

To quantify the scatter in the predicted intrinsic rates we calculate the mean of the ratios between the maximum and minimum predicted rates given by

$$\langle \sigma_{\mu} \rangle = \frac{1}{28} \sum_{xyz=000}^{xyz=333} \frac{\max(\mathcal{R}_{m, Axyz}^0, \dots, \mathcal{R}_{m, Txyz}^0)}{\min(\mathcal{R}_{m, Axyz}^0, \dots, \mathcal{R}_{m, Txyz}^0)}, \quad (3)$$

and

$$\langle \sigma_{xyz} \rangle = \frac{1}{20} \sum_{\mu=A}^{\mu=T} \frac{\max(\mathcal{R}_{m, \mu 000}^0, \dots, \mathcal{R}_{m, \mu 333}^0)}{\min(\mathcal{R}_{m, \mu 000}^0, \dots, \mathcal{R}_{m, \mu 333}^0)}, \quad (4)$$

where we used the short-hand notation $\mathcal{R}_m^0 = \mathcal{R}_m(t_m(z \approx 0))$ and μ and xyz are the stellar evolution and $\mathcal{S}(Z, z)$ labels, respectively. Intuitively, Equation 3 represents the uncertainty range from stellar evolution as averaged over the $\mathcal{S}(Z, z)$ models, whereas Equation 4 represents the uncertainty range from $\mathcal{S}(Z, z)$ as averaged over the stellar evolution models. Large (small) values for σ_{μ} and σ_{xyz} correspond to large (small) impacts by binary star evolution and $\mathcal{S}(Z, z)$ variations, respectively.

3.2.1 BHBH merger rates

We find that the intrinsic merging BHBH rates are predicted to lie in the range $\mathcal{R}_m^{0, \text{BHBH}} \approx 3.8$ –810 $\text{Gpc}^{-3} \text{ yr}^{-1}$ as shown in the top panel in Figure 2. The combined uncertainty thus impacts the predicted rates with a factor of up to⁸ ≈ 210 . We find that the variations in stellar and binary evolution impact the BHBH rate on average with $\langle \sigma_{\mu} \rangle \approx 6$, while variations in our $\mathcal{S}(Z, z)$ models impact the predicted BHBH rate with uncertainties of $\langle \sigma_{xyz} \rangle \approx 20$.

We find that the majority of our stellar and binary evolution model variations do not impact the BHBH rate with more than a factor ≈ 2 , as can be seen in the top panel of Figure 2 when comparing the predicted rates with our fiducial model. Model T ($f_{\text{WR}} = 5$) has the highest impact on the rates. The other largest BHBH rate changes are

⁷ Where we use the WMAP9–cosmology from [Astropy \(Hinshaw et al. 2013\)](#). This assumption does not drastically impact our results.

⁸ This is the ratio between the minimum and maximum predicted rates quoted with the error bar in the left of each panel in Figure 2. This is not the same as multiplying $\langle \sigma_{xyz} \rangle$ and $\langle \sigma_{\mu} \rangle$, as the latter are averages calculated using Equations 3 and 4, and because the impacts from stellar evolution and $\mathcal{S}(Z, z)$ variations are not (fully) independent.

⁶ See our online table [B](#).

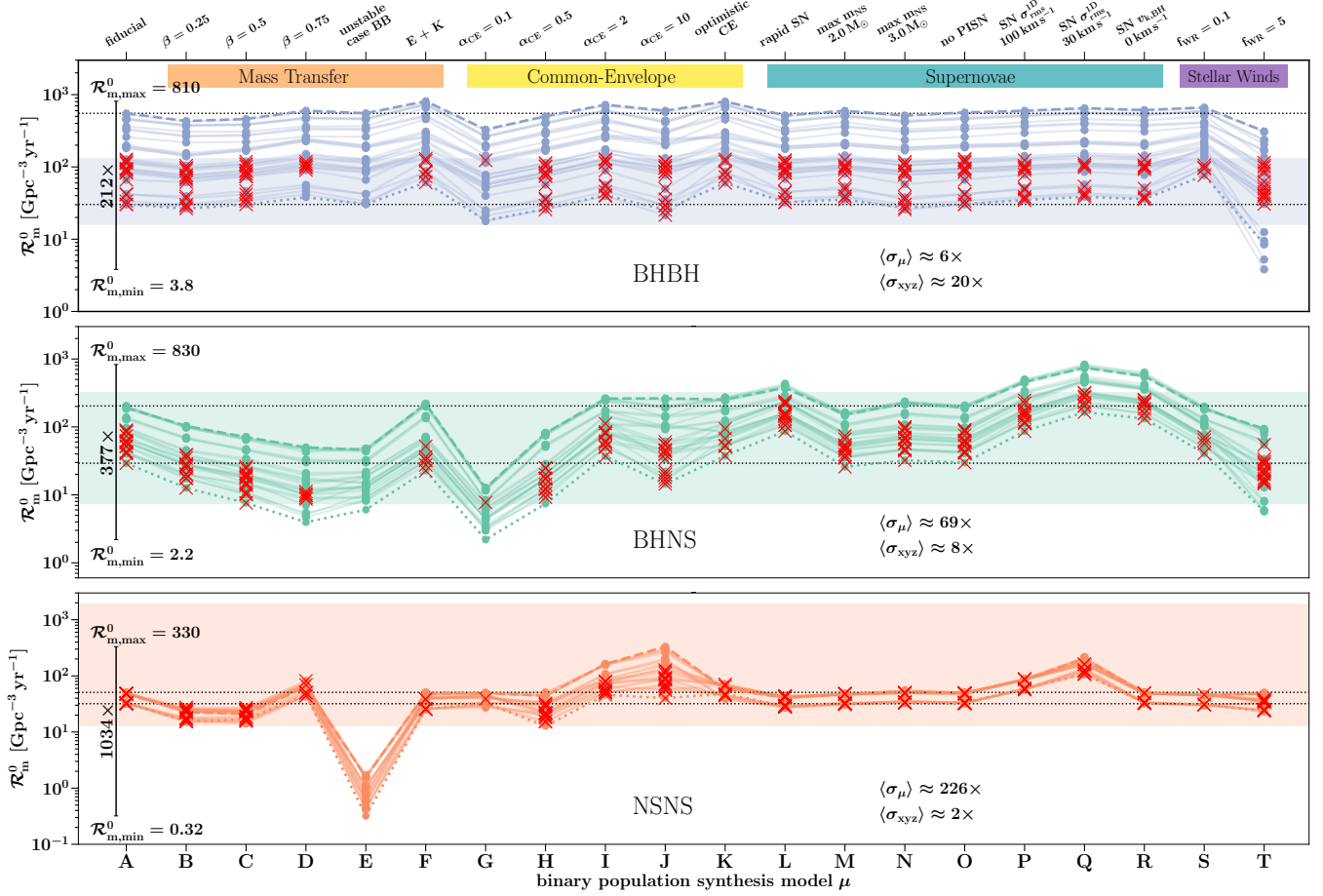




Figure 2. Intrinsic (local) merger rate densities for merging BHBHs (top panel), BHNSs (middle panel) and NSNSs (bottom panel) systems for our 560 model variations. The rates are for merging DCOs at $z \approx 0$ calculated using Equation 2 (i.e., without applying GW detector selection effects). We show for each of the 20 binary population synthesis models (Table 1) the merger rates for the 28 variations in $\mathcal{S}(Z, z)$ (Table A1). We connect predictions that use the same $\mathcal{S}(Z, z)$ model with a line for visual reasons only. Two $\mathcal{S}(Z, z)$ variations are highlighted corresponding to $\mathcal{S}(Z, z)$ models resulting in one of the highest ($xyz=231$, dashed) and lowest ($xyz=312$, dotted) merger rate predictions. The values $\langle \sigma_\mu \rangle$ and $\langle \sigma_{xyz} \rangle$ quote a proxy for the mean scatter (Equations 3 and 4) in the predicted rates due to variations in binary population synthesis and $\mathcal{S}(Z, z)$, respectively. The minimum and maximum rates and their ratio are quoted with a black error bar on the left. We use the short-hand notation $\mathcal{R}_m^0 \equiv (dN_{\text{det}}^2/dt_s dV_c)(t_m(z \approx 0))$. Shaded horizontal bars indicate the ranges spanned by the 90% credible intervals for the intrinsic merger rates inferred from GW observations The LIGO Scientific Collaboration et al. (2021c): $\mathcal{R}_m^{\text{BHBH}} = 16\text{--}130 \text{ Gpc}^{-3} \text{ yr}^{-1}$ (BHBH), $\mathcal{R}_m^{\text{BHNS}} = 7.4\text{--}320 \text{ Gpc}^{-3} \text{ yr}^{-1}$ (BHNS) and $\mathcal{R}_m^{\text{NSNS}} = 16\text{--}1900 \text{ Gpc}^{-3} \text{ yr}^{-1}$ (NSNS). Model realizations where all three of the BHBH, BHNS and NSNS simulated merger rate densities overlap with the inferred ranges from observations are marked with red crosses. A video showing the rates for each individual $\mathcal{S}(Z, z)$ model is provided at <https://youtu.be/LkT7FD1xC2g>. Dashed horizontal lines indicate the range for the fiducial model (A). At the top we added colored labels to indicate what physics assumptions are varied compared to our fiducial assumptions in the models.  

from stellar evolution models that change the CE assumptions (e.g., models F, G and K).

The 90% credible intervals from the GW inferred rate of merging BHBHs spans $\mathcal{R}_m^{\text{BHBH}} = 16\text{--}130 \text{ Gpc}^{-3} \text{ yr}^{-1}$ based on the GWTC-3 catalog from The LIGO Scientific Collaboration et al. (2021c)⁹. Figure 2 shows that only a subset of our $\mathcal{S}(Z, z)$ models (lower lines in the top panel) predict merging BHBH rates that are consistent with this range. The $\mathcal{S}(Z, z)$ realizations that typically over-predict the observed BHBH rate for all stellar evolution models are the ones with an implementation of the Langer & Norman (2006) MZR ($z = 1$). This MZR model corresponds to the lowest average Z among our MZR variations (right panel, Figure A2), which significantly increases the

BHBH yield. The over-prediction is even more significant if other formation channels than the isolated binary evolution channel further contribute to the observed BHBH rate (e.g., Abbott et al. 2021b; Zevin et al. 2021).

3.2.2 BHNS merger rates

For the merging BHNS systems we find rates in the range $\mathcal{R}_m^{\text{BHNS}} \approx 2.2\text{--}830 \text{ Gpc}^{-3} \text{ yr}^{-1}$ as shown in the middle panel of Figure 2. Our combined model variations impact the predicted BHNS rates with an uncertainty factor of up to ≈ 377 . We find that variations in the rate are typically $\langle \sigma_\mu \rangle \approx 69$ for binary evolution variations, while the impact from $\mathcal{S}(Z, z)$ variations typically leads to a range of $\langle \sigma_{xyz} \rangle \approx 8$.

Almost all predicted BHNS rates are consistent with the range $\mathcal{R}_m^{\text{BHNS}} = 7.4\text{--}320 \text{ Gpc}^{-3} \text{ yr}^{-1}$ spanned by the 90% credible in-

⁹ From hereon we quote the rate range from the ‘merged’ row in Table II in The LIGO Scientific Collaboration et al. (2021c) that represents the union of 90% credible intervals from their PDB, MS and BGP models.

tervals from observations (The LIGO Scientific Collaboration et al. 2021c). The exceptions are a few of the $S(Z, z)$ models in combination with models D, E and G that under-predict the BHNS rate and a few of the $S(Z, z)$ models with $z = 1$ in combination with stellar evolution model P, Q and R (lower SN kicks), which slightly over-predict the observed upper limit. The latter models have reduced SNe kicks, which increases the fraction of systems that stay bound during the SN compared to our fiducial model (see Paper I for a more detailed discussion). Future improved constraints might enable ruling out models.

3.2.3 NSNS merger rates

The bottom panel in Figure 2 shows our predicted merging NSNS rates. We find values in the range $\mathcal{R}_m^{0, \text{NSNS}} \approx 0.32\text{--}330 \text{ Gpc}^{-3} \text{ yr}^{-1}$. Combined, our 560 model realizations impact the estimated NSNS rates up to a factor of ≈ 1030 . The uncertainty from stellar and binary evolution dominates the scatter in the calculated NSNS rates (cf., Santoliquido et al. 2021), impacting the rate by $\langle \sigma_\mu \rangle \approx 226$ compared to $\langle \sigma_{xyz} \rangle \approx 2$ when varying the $S(Z, z)$.

All of our calculated NSNS merger rates except those involving model E match the observed merger rate density range of $\mathcal{R}_m^{0, \text{NSNS}} = 16\text{--}1900 \text{ Gpc}^{-3} \text{ yr}^{-1}$ (The LIGO Scientific Collaboration et al. 2021c), although the majority of rates fall in the lower end of the observed NSNS merger rate range. Models I, J, P and Q have the highest predicted NSNS merger rate densities as the NSNS rate is boosted in these models. For example, in models I and J fewer binaries merge during the CE phase compared to the fiducial model. In models P and Q the smaller value for the root-mean-square velocity dispersion reduces the kick velocities that decreases the number of binaries that disrupts during the SN. Only model E is in particular an outlier in the predicted NSNSs merger rate. In this channel the formation yield of merging NSNSs is extremely low (Figure 1). This is because the majority of systems leading to merging NSNSs experience a case BB mass transfer phase that ultra-strips the NS progenitor (Dewi & Pols 2003; Tauris et al. 2017). In our model variation E we assume this phase of mass transfer to be unstable, leading to a stellar merger in combination with our pessimistic CE assumption. Indeed, in model F where we have the same settings as in model E but add the ‘optimistic’ CE assumptions, we obtain NSNS rates consistent with our fiducial model. If we exclude model E we find instead $\langle \sigma_\mu \rangle \approx 10$ (while $\langle \sigma_{xyz} \rangle$ remains unchanged).

3.2.4 Trends with stellar evolution variations

There are a few trends visible in the rates in Figure 2. First, the predicted BHNS rate declines with increasing mass transfer efficiency, β (models B, C and D). The increase in β leads the secondary to accrete more mass during the first stable mass transfer phase, resulting in more massive secondaries and typically larger separations because the mass transfer is more conservative. The larger masses and/or larger separations at higher β values results in more binaries eventually disrupting during a SN, merging during the CE phase, and/or forming a BHBH binary instead of a BHNS (cf., Kruckow et al. 2018). In addition, this also impacts t_{inspiral} in a complex way due to the interplay of the typically larger separation after the first stable mass transfer phase, as well as more orbital shrinking during the CE phase because the star has to eject a more massive envelope.

The BHBH and NSNS rates instead increase with increasing values for β . This different behavior comes from a non-trivial combination of ways in which the formation pathways of binaries leading to merging

BHNSs are different from merging BHBHs and NSNSs and how changing β impacts this. An example is that the impact from β on the evolution of the binary is connected with the mass ratios of the binary (e.g. the mass ratio impacts the size of the Roche lobes, whether the mass transfer is stable or unstable and whether the mass transfer causes the binary orbit to widen or shrink). The merging BHBH and NSNS populations are DCOs with more equal (i.e. $q \sim 1$) mass ratio distributions compared to BHNS (see also §3.4). The binaries that form merging BHBHs and NSNSs originate thus from different mass ratio populations at the same evolutionary stages compared to merging BHNSs. This results in the β parameter impacting the populations differently. Another difference is that the merging BHNS typically form from different formation channels within isolated binary evolution compared to BHBH and NSNS. For example, in our fiducial model (A) a substantial fraction ($\geq 25\%$ of all merging BHBHs in our simulation) of the BHBHs form through only stable mass transfer episodes, without engaging a CE, whereas for BHNSs this is much smaller ($\leq 5\%$). The parameter β has a different impact on each of these formation channels.

Second, the BHNS rate increases with increasing values for α (models G, H, I and J) as a result of more efficient ejection of the CE. This causes typically fewer systems to merge during the CE (cf., Kruckow et al. 2018, Figure 17). On the other hand, the rates slightly decline for the highest α_{CE} values as in this case binaries do not shrink enough to merge in a Hubble time (see also the discussion on α in §3.1.1 from Bavera et al. 2021).

3.3 GW detectable merger rates

The top panel in Figure 3 shows the predicted detectable merger rates for our 560 model variations. These are calculated by volume integrating Equation 2 and taking into account the sensitivity of a GW detector, quantified by the probability P_{det} of observing a merging binary of specified masses at a given redshift and corresponding distance. Here we assume a detector sensitivity comparable to Advanced LIGO in its design configuration (hereafter, design sensitivity; LIGO Scientific Collaboration et al. 2015; Abbott et al. 2020a). We follow Barrett et al. (2018) and choose a detector signal-to-noise ratio threshold of 8 as a proxy for detectability by a GW detector network (e.g., LVK). The detectable merger rate is given by:

$$\mathcal{R}_{\text{det}}(t_{\text{det}}, m_1, m_2) = \frac{d^3 N_{\text{det}}}{dt_{\text{det}} dm_1 dm_2} = \int dV_c \frac{dt_m}{dt_{\text{det}}} \frac{d^4 N_{\text{merger}}}{dt_m dV_c dm_1 dm_2} P_{\text{det}}(m_1, m_2, z), \quad (5)$$

where t_{det} is the time in the detector (i.e., the observer) frame, and m_1 and m_2 are the component masses of the DCO in the source frame (see Paper I for further details).

Considering the 560 model variations we find predicted detected rates for an LVK detector network at design sensitivity in the range $\mathcal{R}_{\text{det}}^{\text{BHBH}} \approx 17\text{--}12000 \text{ yr}^{-1}$, $\mathcal{R}_{\text{det}}^{\text{BHNS}} \approx 0.36\text{--}180 \text{ yr}^{-1}$ and $\mathcal{R}_{\text{det}}^{\text{NSNS}} \approx 0\text{--}12 \text{ yr}^{-1}$, as shown in the top panel of Figure 3. We find that the stellar, binary, and cosmic evolution combined impact the predicted detectable merger rates by factors of up to $\approx 500\text{--}1300$. This is slightly higher compared to the intrinsic rates as the detectable population is biased to higher masses, where our simulations are relatively more sensitive to stellar evolution and $S(Z, z)$ assumptions.

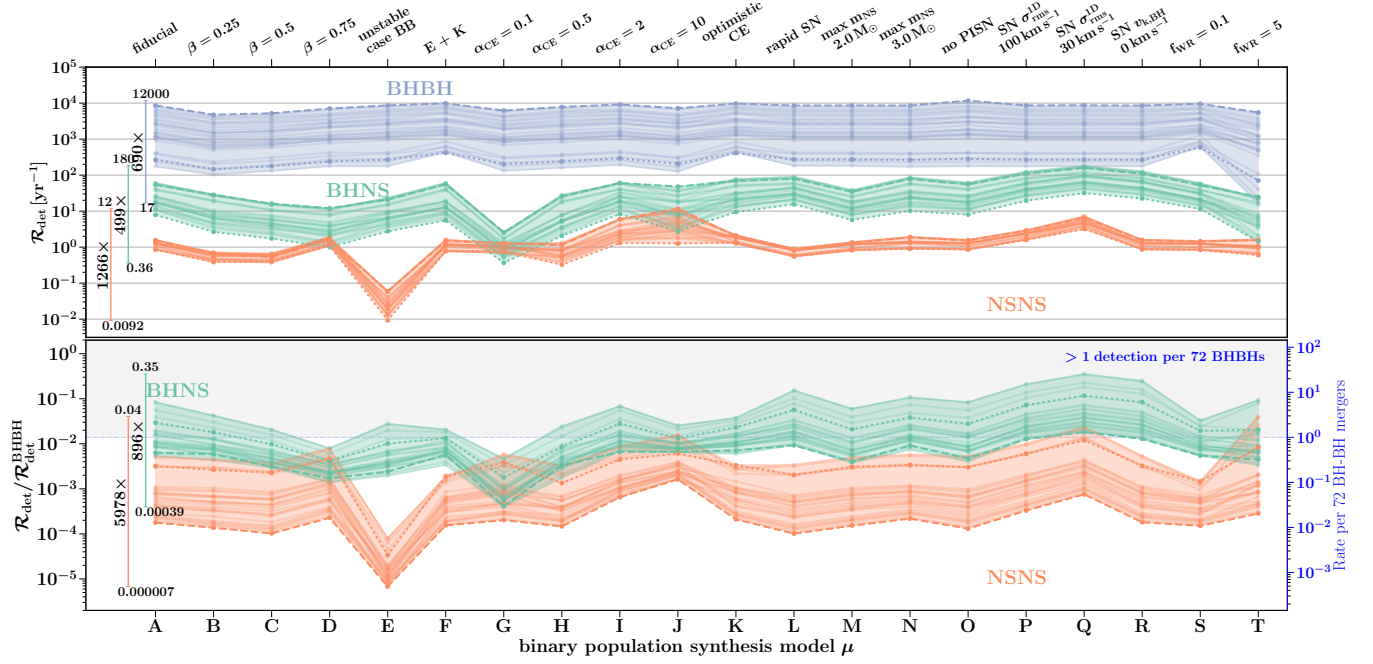


Figure 3. Top panel: The calculated detectable merger rates for merging BHBH (blue), BHNS (green) and NSNS (orange) for a GW network at design sensitivity for our 560 models. **Bottom panel:** The predicted merging BHNS and NSNS detectable rate ratios over merging BHBH. On the right axes we scale the ratios to the 72 BHBH detections with false-alarm rate $\leq 1 \text{ yr}^{-1}$ from the GWTC-3 (The LIGO Scientific Collaboration et al. 2021c). **Both panels:** The layout, lines and symbols are as in Figure 2. We note that the relative rates could be slightly, but not significantly, different at O1-O2-O3 (GWTC-3) sensitivity compared to design sensitivity.

3.3.1 Relative merger rates

The bottom panel of Figure 3 shows the relative merger rates between the different DCO channels for LVK at design sensitivity. We find that almost all of our models predict a higher BHNS detection rate compared to the NSNS detection rate, except for model D (which has a mass transfer efficiency of $\beta = 0.75$) and model G (which assumes $\alpha_{\text{CE}} = 0.1$) in which a subset of the $\mathcal{S}(Z, z)$ models lead to higher NSNS detection rates. The higher BHNS rate is a result from both the high intrinsic yield of BHNS mergers compared to NSNS mergers (Figure 1) and the larger detection volume for BHNS compared to NSNS mergers as a result from their larger masses (§3.4).

3.4 GW detectable mass distribution functions

The uncertainties in stellar and binary evolution and $\mathcal{S}(Z, z)$ also impact the shapes of the mass distributions of detectable DCO mergers, in addition to the overall merger rate densities. We show this in Figures 4 (BHBH), 5 (BHNS) and 6 (NSNS) for our 560 model realizations. Each Figure shows the normalized distributions for the DCO component masses m_1 and m_2 , chirp mass $\mathcal{M}_c = (m_1 m_2)^{3/5} / (m_1 + m_2)^{1/5}$, and mass ratio $q = m_1 / m_2$, where we use subscripts ‘1’ and ‘2’ to indicate the more massive and less massive component in the double compact object system, respectively. To compare the shapes we show kernel density distributions for the chirp mass and summary statistics (i.e., median, 50, 90 and 99 distribution percentiles) for the individual masses, chirp mass and mass ratio for the BHBH, BHNS and NSNS mergers. All distributions are weighted for the detection volume and sensitivity of LVK at design sensitivity using Equation 5 and given by the differential

detectable merger rate $d^2 N_{\text{det}} / dt_{\text{det}} dx$, with x being one of the mass parameters mentioned above.¹⁰

3.4.1 Impact from binary star and cosmic evolution on the distribution shapes

We qualitatively compare the impact on the shape of the detectable mass distributions from variations in stellar and binary evolution and variations in $\mathcal{S}(Z, z)$ by analyzing how the distributions (and distribution statistics) vary; see Figures 4, 5 and 6. Distributions that are similar between vertical panels (different colors) indicate that changes in stellar and binary evolution assumptions do not significantly impact the distribution shape. On the other hand, distributions that are similar between variations plotted within one sub-panel indicate these $\mathcal{S}(Z, z)$ realizations do not significantly impact the shape of the distributions. By comparing these two effects directly we can qualitatively analyze which of the two uncertainties dominates the shape of the detectable mass distributions.

For merging BHBH systems we find that the uncertainty in the shape of the mass distribution is significantly impacted by both variations in stellar evolution and the $\mathcal{S}(Z, z)$. The impact from the $\mathcal{S}(Z, z)$ reflects the metallicity dependence of BHBH formation (§3.1), which also strongly impacts the resulting BH masses (cf., Belczynski et al. 2010; Giacobbo & Mapelli 2018). For example, the peak in the detectable BHBH chirp mass distribution around 30–35 M_{\odot} that is visible in the majority of models in Figure 4 disappears in a small subset of the $\mathcal{S}(Z, z)$ models. These are the $\mathcal{S}(Z, z)$ models with the Panter et al. (2004) GSMF and Ma et al. (2016) MZR ($xyz = 113$,

¹⁰ From hereon we will use the short notation $d\mathcal{R}_{\text{det}}/dx$ for this differential detection rate that describes the ‘shape’ of the distributions.

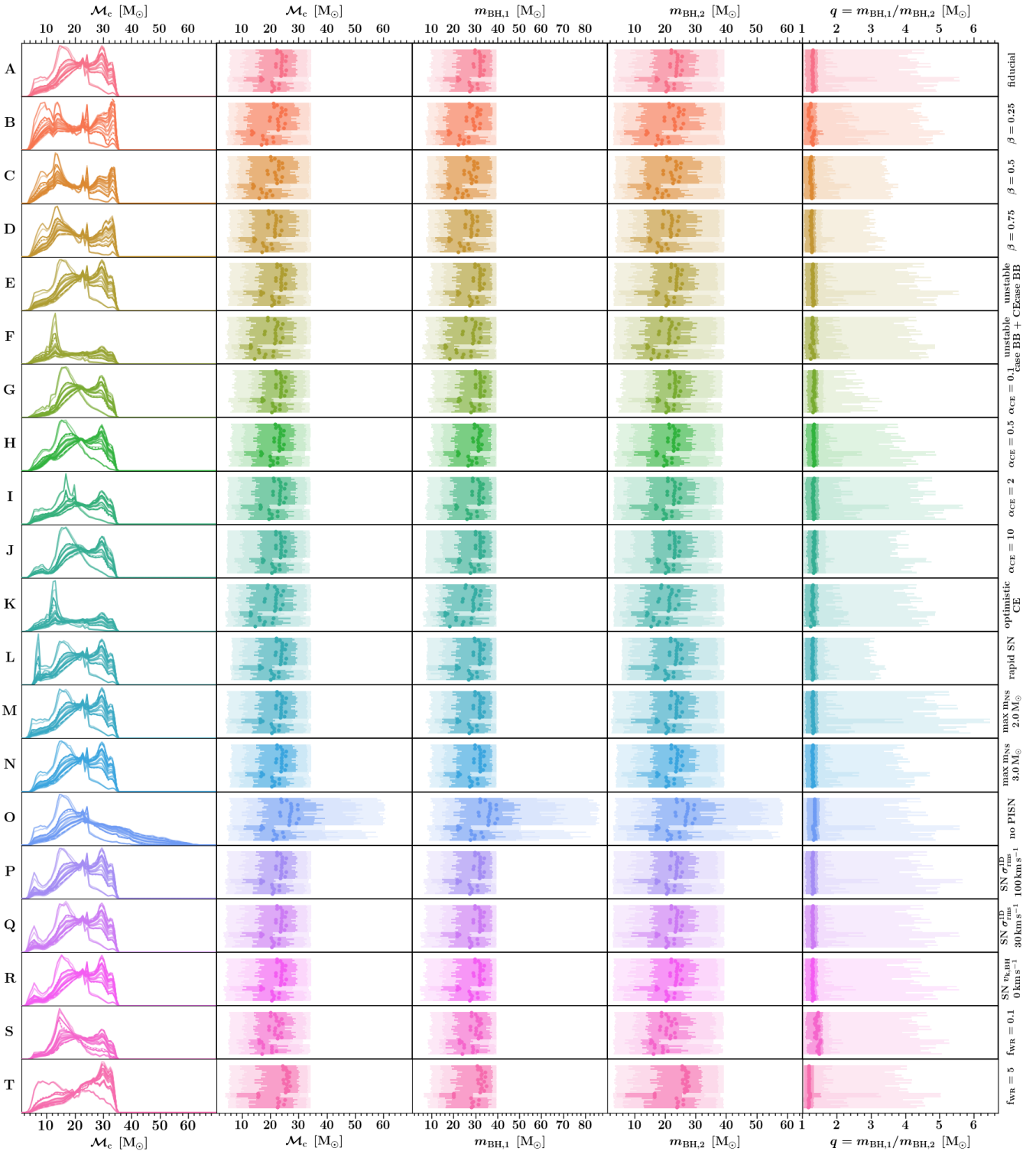




Figure 4. Shape of the detectable mass distribution functions for BHBH mergers from our 560 model realizations. **First column:** the probability distribution functions of the chirp mass \mathcal{M}_c at the time of merger. The distributions are normalized within each panel and given by $d\mathcal{R}_{\text{det}}/dx = (d^2 N_{\text{det}}/dt_{\text{det}} dx)$ for parameter x (A variation of Equation 5). **Other columns:** From left to right we show the chirp mass, the primary (most massive) and secondary (least massive) BH mass, and the mass ratio. In each sub-panel we show 28 individual horizontal bars that visualize the median (scatter points) and the 50%, 90% and 99% (three shades) distribution intervals. A zoom-in that shows the order of the $\mathcal{S}(Z, z)$ models is given in Figure A3. **Rows:** From top to bottom, the panels/colors show the 20 different stellar evolution simulations from Table 1. Within each sub-panel we show the 28 $\mathcal{S}(Z, z)$ models with different lines (first column) or horizontal bars (other columns).  

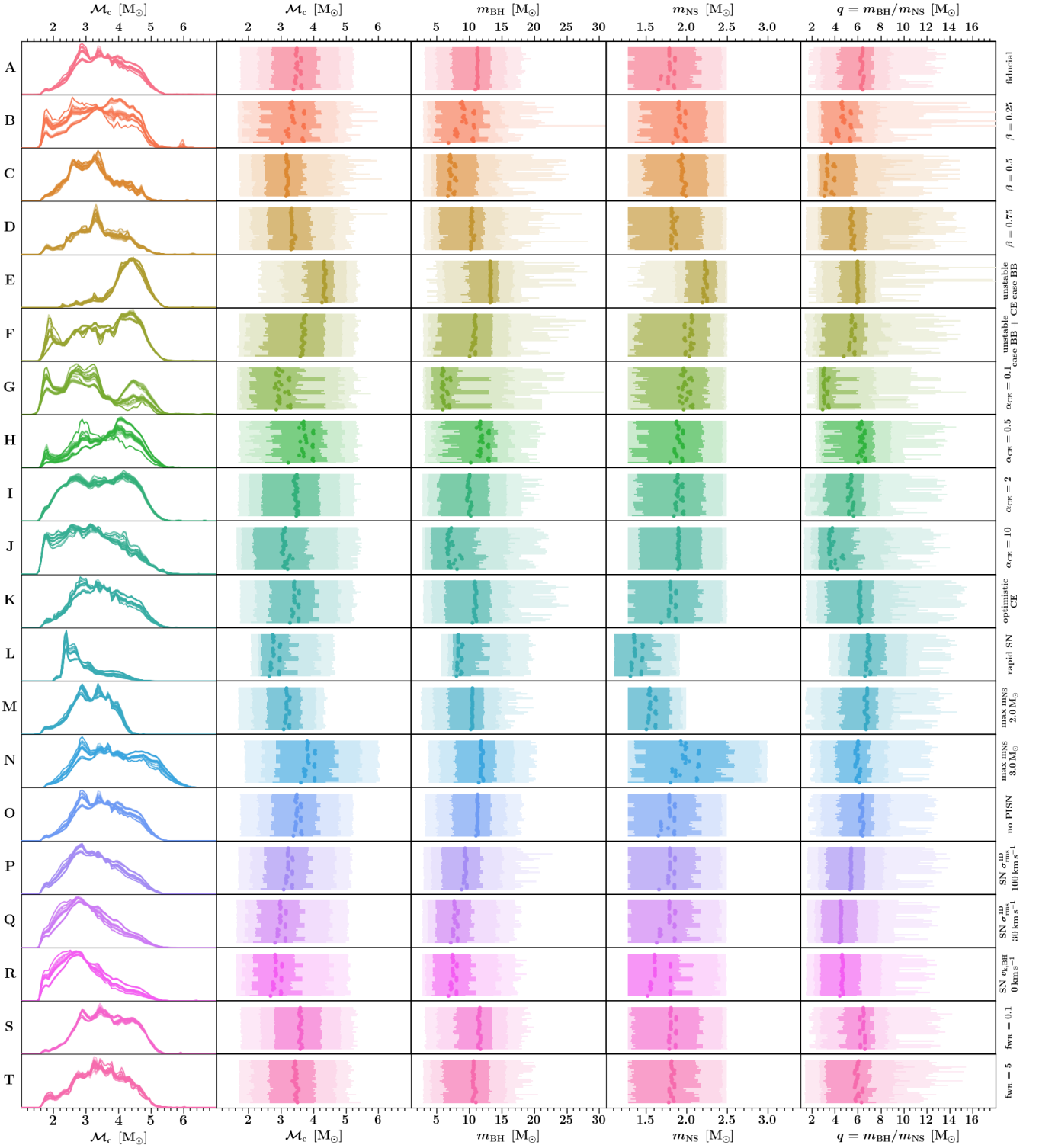




Figure 5. Same as Figure 4 for detectable BHNS mergers. For the individual masses we show the BH (m_{BH}) and NS (m_{NS}) masses.  

213 and 313), which correspond to realizations with high average metallicities compared to the other $S(Z, z)$ models (see Figure B1 in Paper I) and lead to fewer massive BHBH mergers. The stellar and binary evolution variation that impacts the mass distributions most drastically is the model in which we assume pair-instability SNe do not occur (model O), leading to the formation of BHs with masses

$\geq 40 M_{\odot}$. This model assumption may be unrealistic (e.g., Woosley 2017; Farmer et al. 2019). Other significant changes, best visible in the kernel density functions (left-most column in Figure 4), are present for models K (optimistic CE), L (rapid SN remnant model) and T ($f_{\text{WR}} = 0.1$), where, for example, the chirp mass peaks shift, disappear or are created compared to the fiducial model A (e.g., in

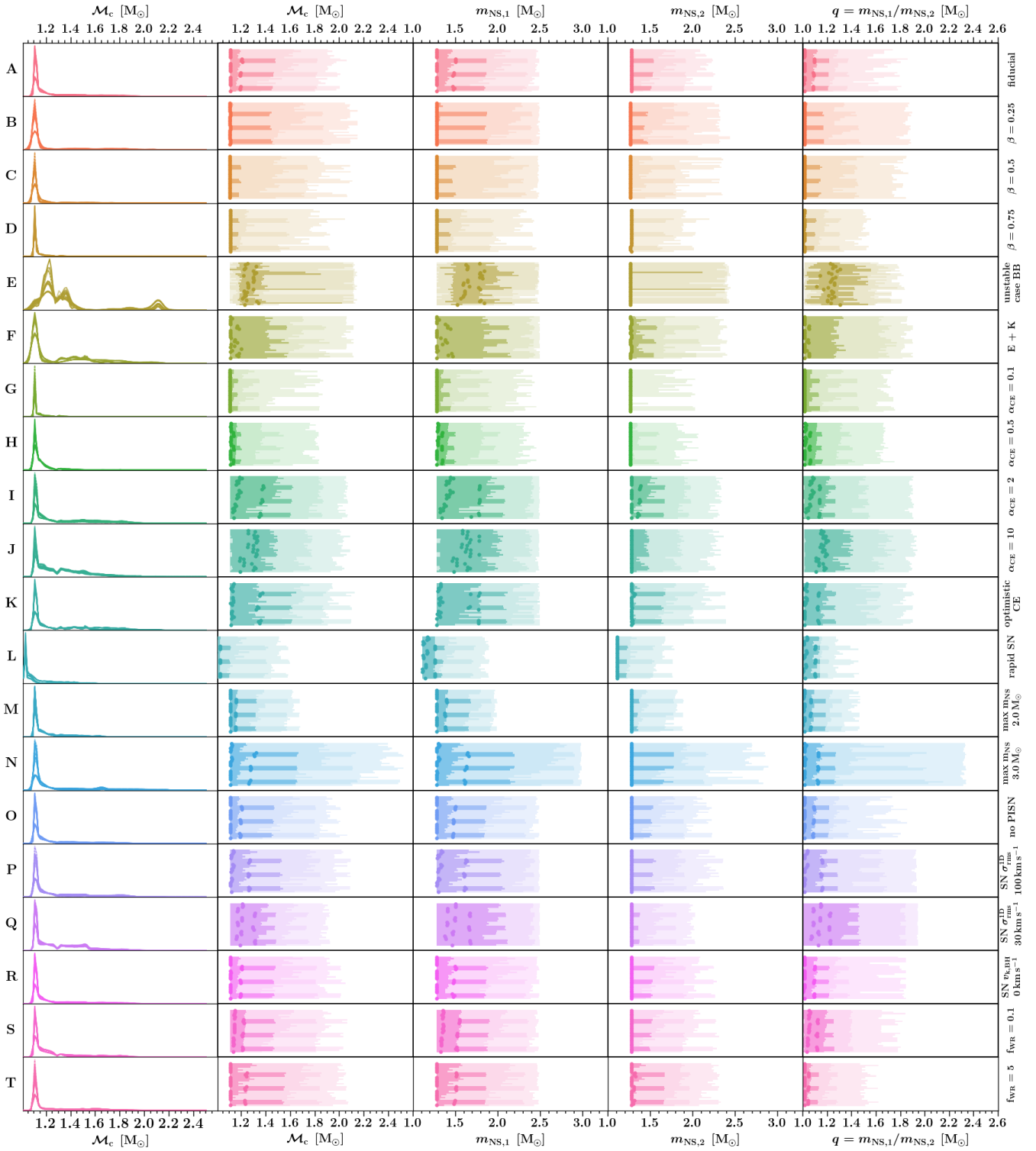



Figure 6. Same as Figure 4 for detectable NSNS mergers. For the individual masses we show the primary (most massive, $m_{\text{NS},1}$) and secondary (least massive, $m_{\text{NS},2}$) NS mass. The shape of model E (unstable case BB) suffers significantly from sampling noise due to the low number of NSNS systems in this variation. 

the ‘optimistic CE’ model due to the many additional BHBH systems added around lower chirp masses).

For merging BHNS systems, on the other hand, the distribution shapes are predominantly impacted by the stellar and binary evolution model variations compared to the $S(Z, z)$ variations (Figure 5).

Primary effects include models E (unstable case BB), L (rapid SN), M (max $m_{\text{NS}} = 2 M_{\odot}$) and N (max $m_{\text{NS}} = 3 M_{\odot}$), where the median and distribution percentiles are visibly different compared to the fiducial model A. Our $S(Z, z)$ variations do not significantly impact

the distribution shapes (i.e. changing $d\mathcal{R}_{\text{det}}/dx$ more than a factor 2) for most of the models except model B, G and H.

For NSNS systems the shape of the normalized mass distributions are impacted by both sets of variations (Figure 6). Among the binary stellar evolution variations, the models that impact the shape of the distribution significantly are realizations that change the SN remnant mass or kick velocity, and/or the CE efficiency (models G, H, I, J, K, L, M, N, P and Q). The distributions from model E (unstable case BB mass transfer) are dominated by sampling noise as a result of the low NSNS yield in this model (§3.1). For the $\mathcal{S}(Z, z)$ particularly all our models with the Langer & Norman (2006) MZR model ($z = 1$) significantly impact the NSNS mass distributions, shifting the distributions to higher median masses in the panels of Figure 6.

In summary, we find that for BHNSs, the variations in the distribution shapes are typically dominated by stellar and binary evolution assumptions, suggesting that observations of BHNS systems could aid in constraining stellar evolution models. For merging BHBH and NSNS the distribution shapes are impacted by both sets of variations (Figures 4 and 6). We therefore argue that constraining stellar evolution or $\mathcal{S}(Z, z)$ models solely from the distribution shapes of merging BHBHs or NSNSs may be challenging. We discuss this further in §4.

3.4.2 Distribution properties considering all model realizations

In the previous section we showed that the model uncertainties in binary and stellar evolution, and $\mathcal{S}(Z, z)$ can significantly impact the shapes of the DCO mass distributions. Here we instead discuss several specific examples of features in the mass distributions in Figures 4, 5 and 6 that are robust across all 560 model variations explored in this work.

- First, in all 560 model variations 95% (99%) of the detectable BHBH mergers have mass ratios $q \lesssim 4$ ($q \lesssim 6$) (right-most column in Figure 4). The BHBH distribution medians and percentiles furthermore indicate that in all model variations BHBHs from isolated binary evolution prefer order unity mass ratios. Detecting a significant fraction ($\gtrsim 5\%$) of BHBH mergers with large mass ratios ($q \gtrsim 5$) would point to other formation pathways or missing physics in our simulations. This is consistent with the 72 BHBH detections announced by LVK with a false alarm rate $< 1 \text{ yr}^{-1}$, which most of are inferred to have mass ratios consistent with unity (The LIGO Scientific Collaboration et al. 2021b). However, the BHBH merger GW190412 ($1/q = 0.28^{+0.12}_{-0.07}$; Abbott et al. 2020b) and the BHBH merger candidate GW190814 ($1/q = 0.112^{+0.008}_{-0.009}$; Abbott et al. 2020d), if common, could hint to the existence of a population with more extreme mass ratios (see also Arca Sedda 2021; Lu et al. 2021; Zevin et al. 2020a, and references therein).

- Second, $\gtrsim 95\%$ of all BHBH mergers are expected to contain a BH with $\gtrsim 8 M_{\odot}$ in all 560 model variations (third column of Figure 4). This is not the case for BHs in BHNS systems where typically $\gtrsim 25\%$ of the detectable mergers are expected to contain a BH of $\lesssim 8 M_{\odot}$ (Figure 5). Our models predict the secondary BH in the population of detected BHBH mergers to also commonly be massive ($\gtrsim 8 M_{\odot}$), although many of our models do allow for at least $\gtrsim 25\%$ of the BHBH mergers to contain a secondary BH with $\lesssim 10 M_{\odot}$. For the currently reported BHBH detections by LVK with a false alarm rate $< 1 \text{ yr}^{-1}$ (but even for those with a false alarm rate $< 0.25 \text{ yr}^{-1}$) all of the inferred medians of the primary BH mass have BH masses $m_{\text{BH},1} \gtrsim 8 M_{\odot}$ (The LIGO Scientific Collaboration et al. 2021c, Table I), consistent with our models.

- Third, in all 560 model variations $\lesssim 5\%$ of the detectable merging BHNS systems have BH masses $m_{\text{BH}} \gtrsim 18 M_{\odot}$ (third column

of Figure 5). As discussed in Paper I, this is due to the fact that more equal mass stars more readily survive important stellar evolution phases in the formation pathways to BHNS mergers; to form a BHNS one of the stars needs to be of sufficiently low mass to form a NS, leading to a preference for the other star to also be of lower mass than is typical in BHBH. Consequently, we find that in all our 560 model realizations $\lesssim 5\%$ of BHNS mergers have chirp masses of $\gtrsim 5.5 M_{\odot}$. This suggests that detecting a BHNS merger with a BH mass $m_{\text{BH}} \gtrsim 18 M_{\odot}$ could indicate that the system did not form from isolated binary evolution processes our models include, but instead from chemically homogeneous evolution and/or dynamical formation where such high BH masses are more commonly expected (e.g., Marchant et al. 2017; McKernan et al. 2020; Rastello et al. 2020). The two detected BHNS systems with a false alarm rate $< 1 \text{ yr}^{-1}$, GW200105 and GW200115, have $\mathcal{M}_c \lesssim 3.5 M_{\odot}$ (at the 90% credible interval) (Abbott et al. 2021c) consistent with our models (see also Broekgaarden & Berger 2021; Broekgaarden et al. 2021).

- Fourth, we find that in all 560 model variations the NSs in detectable NSNS mergers typically have lower NS masses compared to those in detectable BHNS mergers (Figures 5 and 6). We find this is true for both NS components in the NSNS mergers. This is again due to the preference for equal mass binaries to survive important evolutionary phases leading to BHNS formation, thereby favoring more massive pre-NS stars to form a BHNS system (see Paper I for more details). To date two NSNS and BHNS detections have been announced by LVK with a false alarm rate $< 1 \text{ yr}^{-1}$ (The LIGO Scientific Collaboration et al. 2021c). For the NSNS detections the NS masses are $m_{\text{NS},1} = 1.46^{+0.12}_{-0.10}$ and $m_{\text{NS},2} = 1.27^{+0.09}_{-0.09}$ (GW170817; Abbott et al. 2017) and $m_{\text{NS},1} = 2.0^{+0.6}_{-0.3}$ and $m_{\text{NS},2} = 1.4^{+0.3}_{-0.3}$ (GW190425; Abbott et al. 2020c), which may indicate a NSNS mass distribution that is not consistent with Galactic NSNS observations (e.g. Vigna-Gómez et al. 2018; The LIGO Scientific Collaboration et al. 2021c). For the BHNS detections the NS masses were found to be $m_{\text{NS}} = 1.9^{+0.3}_{-0.2} M_{\odot}$ (GW200105) and $m_{\text{NS}} = 1.5^{+0.7}_{-0.3} M_{\odot}$ (GW200115) (Abbott et al. 2021c). More detections are needed to calculate robust median NS masses in NSNS and BHNS detections.

Besides the four specific points above, more common trends throughout our 560 model variations are visible in Figures 4, 5 and 6, particularly in the lower and upper bounds for the BH and NS masses. Several of these trends, however, are direct results from the remnant mass prescriptions used in our models. For example, all models with the exception of model O (no PISN) predict that 90% of the detected BHBH mergers have chirp masses in the range $\mathcal{M}_c \approx 5\text{--}35 M_{\odot}$. The upper limit is set by the maximum possible BH masses of $\sim 40 M_{\odot}$ allowed due to the implementation of pair-instability SN in our models (e.g., Marchant et al. 2019; Stevenson et al. 2019); in model O we do not implement pair-instability SNe, and find BH masses up to about $80 M_{\odot}$ and BHBH chirp masses up to about $60 M_{\odot}$. In addition, in most of our model realizations the majority of NSs in NSNS mergers have masses of $\approx 1.3 M_{\odot}$ (consistent with e.g., Tauris et al. 2017; Vigna-Gómez et al. 2018). This is because many NSNS experience at least one electron-capture SN (ECSN), which in COMPAS are mapped to a mass of $1.26 M_{\odot}$ (Timmes et al. 1996, Team COMPAS: J. Riley et al. 2021). In addition, many NSNS mergers in our models originate from relatively low mass stars with carbon-oxygen cores of $\lesssim 2.5 M_{\odot}$ at the time of the SN, which in the delayed SN remnant mass prescription are mapped to a fixed value of $m_{\text{NS}} \approx 1.28 M_{\odot}$ (Fryer et al. 2012). Combined, this results in a peak of NSs masses at $m_{\text{NS}} \approx 1.3 M_{\odot}$. Exceptions to this are the rapid SN remnant mass model (model I) where these low mass stars are instead mapped to NS masses of $\approx 1.1 M_{\odot}$ leading to a broader peak

at $\approx 1.1 - 1.3 M_{\odot}$. The lower and upper NS limits are also artificially set in our models to $\approx 1 M_{\odot}$ and $\approx 2.5 M_{\odot}$, respectively (cf., [Fryer et al. 2012](#)), except in models M and N where we set the upper limit to $2 M_{\odot}$ and $3 M_{\odot}$, respectively.

3.5 Delay time and birth metallicity distributions

The uncertainties in the stellar evolution and $\mathcal{S}(Z, z)$ prescriptions in population synthesis modelling can also impact the expected delay time (t_{delay}) and birth metallicity (Z) distributions of the detectable DCO mergers. We show the impact from the 560 model realizations explored in this study in Figures 7, 8 and 9. We focus on the t_{delay} and Z distributions as these properties can be (indirectly) constrained from observations (e.g., [Im et al. 2017](#); [Safarzadeh et al. 2019](#); [Fishbach & Kalogera 2021](#)). In addition, these distributions provide insights into the range of birth metallicities and star formation redshifts that current GW observations probe, which can be informative for future modelling (e.g., help understand where to focus computational time and which Z to simulate). We note that impacts on the t_{delay} distribution also impact (indirectly) the distribution of Z , because the birth metallicity distribution (dP/dZ ; §2.2) evolves as a function of redshift.

The most striking feature of the t_{delay} and Z distributions is that both are significantly impacted by the $\mathcal{S}(Z, z)$ variations for all three DCO merger types. This is particularly discernible in the large scatter of the distribution percentiles (see each sub-panel). We find that the impact from $\mathcal{S}(Z, z)$ models is particularly significant for our variations in the choice of the metallicity probability function (dP/dZ), which describes the distribution of birth metallicities of stars at a given redshift. This is because the birth metallicity strongly impacts the properties and rate of the DCO mergers, including through the metallicity-dependent formation yields, through mass loss that impact the DCO masses and can widen the orbit of the binary, and through the metallicity-dependent radial expansion of stars, which impacts mass transfer phases in our models (§3.1). In the convolution to obtain the detectable DCO mergers in Equation 5 all of these properties impact the resulting population. Thus, the t_{delay} and Z distributions of the detectable DCO mergers are significantly impacted by the choice of (dP/dZ) and $\mathcal{S}(Z, z)$.

Variations in the stellar and binary evolution assumptions can also significantly impact the t_{delay} and Z distributions. For example, model T ($f_{\text{WR}} = 5$), which increases the mass loss through stellar winds, drastically suppresses the number of BHBH and BHNS events that can form at higher metallicities ($\log(Z) \gtrsim -2.5$), thereby leading to fewer of the detectable BHBH and BHNS mergers forming from these metallicities (Figures 7 and 8). Another example is Model J ($\alpha_{\text{CE}} = 10$), which results in longer t_{delay} and lower Z compared to our fiducial model in Figures 8 and 9. In model J orbital angular momentum of the binary can much more efficiently be transformed into ejecting the CE. This leads to less orbital shrinking during the CE phase and longer inspiral times. As a result only BHNSs and NSNSs that formed early in the Universe with low Z have had long enough the time to inspiral and be detectable today. Model J does not impact the BHBH distributions as significantly because most detectable BHBH mergers in our simulations only go through stable mass transfer phases (as these produce more massive BHBHs in our simulations that the detectable population is biased to, cf. [van Son et al. 2021](#)).

Overall, we find that the delay time distributions span a broad range between a few Myr and the Hubble time with possible peaks both at short (< 1 Gyr) and long (> 5 Gyr) delay times, reflecting contributions from binaries born at lower and higher redshifts, re-

spectively. This is a result from the interplay between the $\mathcal{S}(Z, z)$ being a function of redshift in combination with the DCO properties and formation efficiencies being Z dependent. We find that our model variations indicate that the detectable BHBH mergers (Figure 7) probe systems with the longest median delay times, compared to BHNS and NSNS mergers (Figures 8 and 9). However, exceptions exist, including model J ($\alpha_{\text{CE}} = 10$) where the median delay times of detected BHNS and NSNS mergers are larger than those of BHBH mergers for the reasons discussed above.

For the birth metallicity distribution shapes the right panels of Figures 7, 8 and 9 show that the detectable DCO mergers arise from a broad range of birth metallicities. As expected from the formation yield efficiencies, BHBH mergers typically originate from the lowest birth metallicities, with most of our models having a median $\log_{10}(Z)$ of $\lesssim -2.5$, whereas the detectable BHNS and NSNS populations originate in our models from higher Z with most models having median $\log_{10}(Z)$ of $\gtrsim -2.5$.

4 DISCUSSION

4.1 A realistic view of population synthesis models

In this paper we demonstrate the importance of considering the uncertainties in both massive star and binary evolution, as well as the $\mathcal{S}(Z, z)$ when aiming to learn about the formation, evolution, and mergers of binaries through a comparison of population synthesis models to GW observations. Here we discuss the implications of our results for interpreting population synthesis studies.

On the one hand, our findings provide a cautionary note for using GW observations to uncover stellar and binary evolution properties. Studies that draw conclusions by comparing population synthesis results with GW observations without considering the wide range of uncertainties in both stellar/binary evolution and $\mathcal{S}(Z, z)$ assumptions could be drastically biased by the specific model realization that is chosen to derive the results (cf. [Belczynski et al. 2021](#); [Bouffanais et al. 2021](#)). For example, studies including [Zevin et al. \(2017\)](#), [Bouffanais et al. \(2019\)](#), [Franciolini et al. \(2021\)](#), [Ng et al. \(2021\)](#) and [Zevin et al. \(2021\)](#) aim to determine the contributions of different formation channels to the observed BHBH population. Further examples include [Fragione \(2021\)](#), which estimates the number of BHNS mergers with an electromagnetic counterpart. Our work shows that uncertainties in both stellar and binary evolution and $\mathcal{S}(Z, z)$ modelling can drastically impact the rate and distribution shapes of the BHBH, BHNS and NSNS populations, challenging the ability to draw strong conclusions when only considering a few population synthesis models at this stage.

The situation is even more complex when considering that our larger suite of models (560 realizations) still only represents a subset of the overall uncertainties in population synthesis studies. For example, even our broader set of models does not account for uncertainties in the stellar evolution tracks (e.g., [Laplace et al. 2020](#); [Agrawal et al. 2020](#)), internal mixing (e.g., [Schootemeijer et al. 2019](#)), stellar rotation (e.g., [de Mink & Mandel 2016](#); [Mapelli et al. 2020](#)), the more complex physics of the CE phase (e.g., [Klencki et al. 2021](#); [Ivanova et al. 2020](#); [Marchant et al. 2021](#); [Olejak et al. 2021](#)), the additional possible remnant mass prescriptions (e.g. [Dabrowny et al. 2021](#); [Mandel et al. 2021](#)), the initial conditions of binary systems (e.g., [de Mink & Belczynski 2015](#); [Moe & Di Stefano 2017](#); [Klencki et al. 2018](#)), and the possible contributions from other formation channels (e.g., [Zevin et al. 2021](#)). In addition, there are $\mathcal{S}(Z, z)$ model variations that we did not explore, including alternative analytical

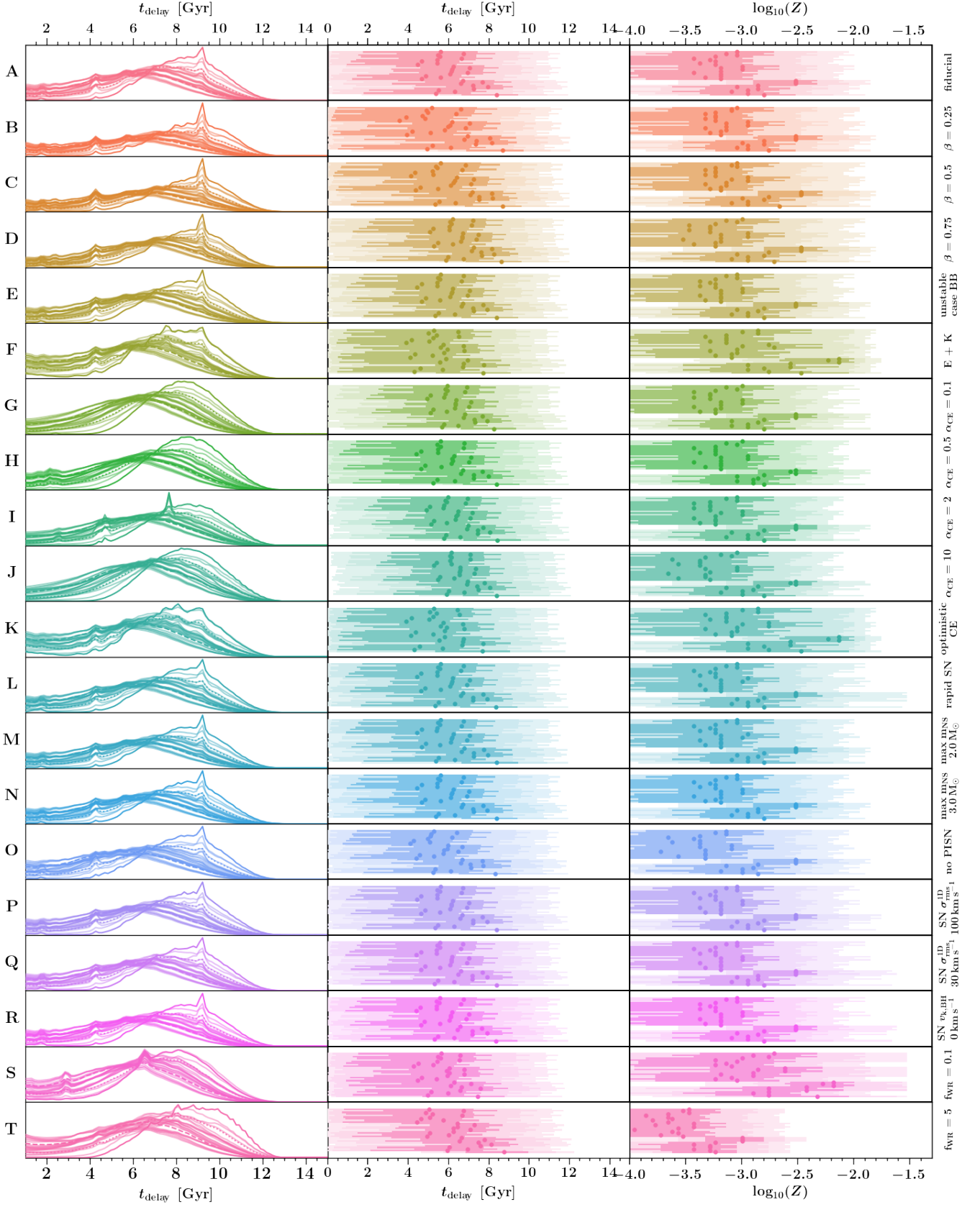


Figure 7. The delay time t_{delay} and birth metallicity Z distributions for detectable BHB mergers for our 560 model realizations. The distributions and percentiles are plotted as in Figure 4. The delay time is the time since formation of the binary system at the zero-age main sequence until the moment of merger. [B](#) [E](#)

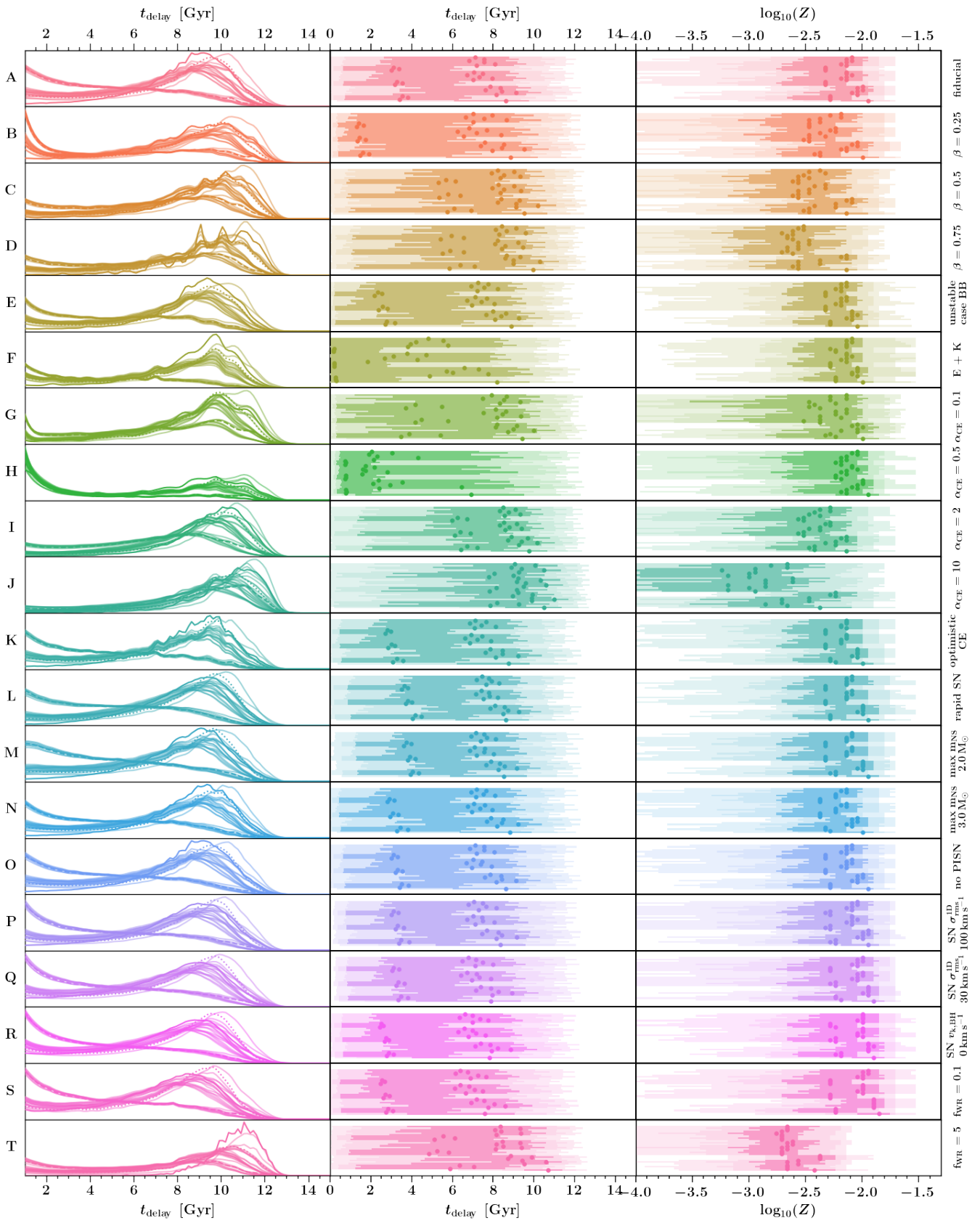



Figure 8. Same as Figure 7 for detectable BHNS mergers. 

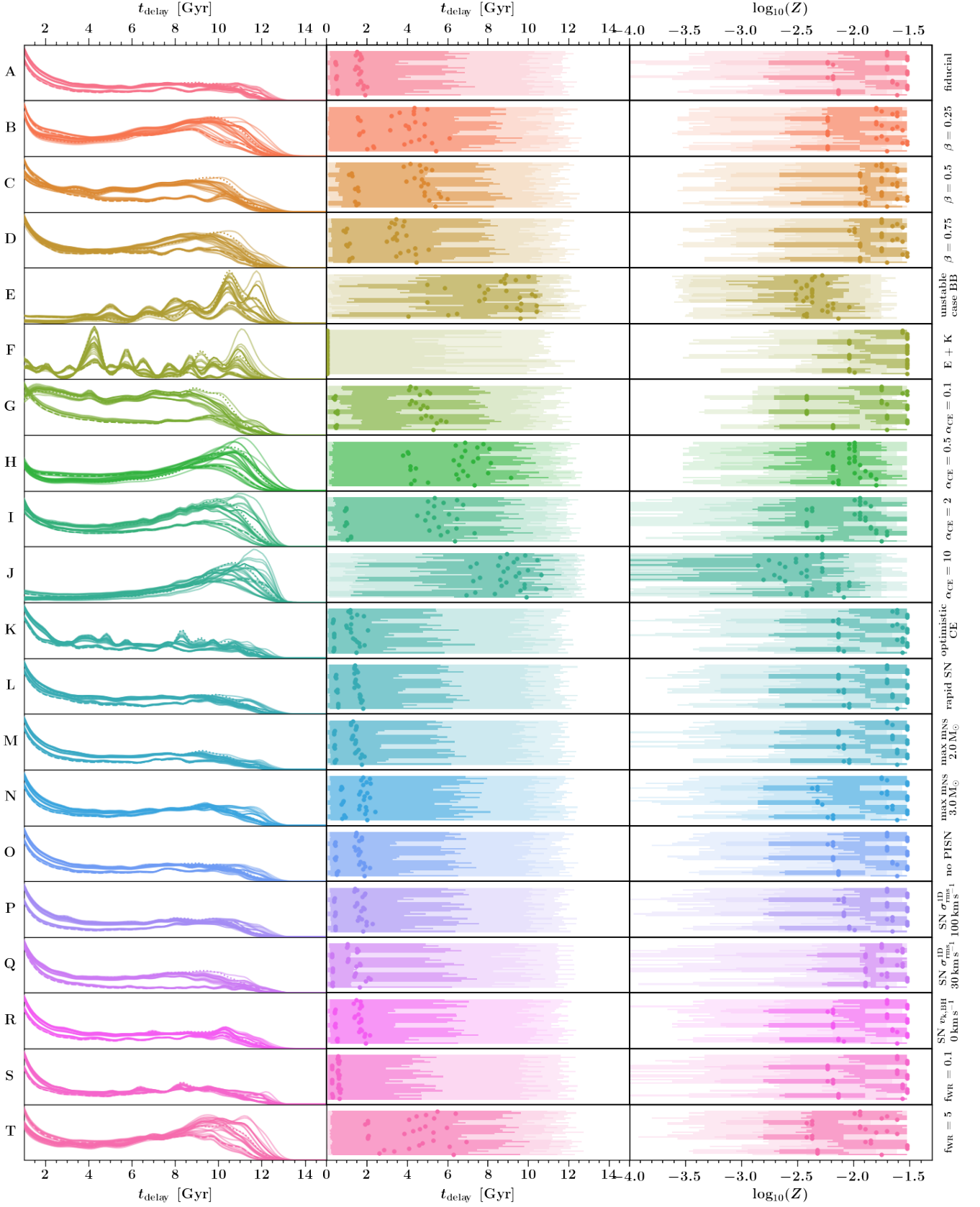


Figure 9. Same as Figure 7 for detectable NSNS mergers. The shape of model E (unstable case BB) suffers significantly from sampling noise due to the low number of NSNS systems in this variation (and similarly for model F). [☒](#) [☒](#)

prescriptions (e.g., [Chruślińska et al. 2019](#); [Tang et al. 2020](#)), prescriptions derived from cosmological (zoom-in) simulations (e.g., *FIRE*, *Illustris*, *EAGLE*, *Millennium*; [Lamberts et al. 2016](#); [Mapelli et al. 2017](#); [du Buisson et al. 2020](#); [Briel et al. 2021](#); [Chu et al. 2021](#)), and prescriptions inferred more directly from observations (e.g., [Chruślińska & Nelemans 2019](#); [Chruślińska et al. 2021](#)).

On the other hand, the fact that model predictions are sensitive to the model assumptions also has positive consequences. As the true DCO merger rates and properties become more constrained by observations, then identifying which models are inconsistent with reality aids in excluding some combinations of model assumptions, and so helps to constrain stellar evolution and cosmic history. To do this we need to sufficiently understand how the uncertainties in our assumptions affect the model output. The results in this paper show that simultaneously modelling the impact of uncertainties from stellar evolution and $\mathcal{S}(Z, z)$ on the rates and distribution shapes of all three DCO merger types can help. For example, in §3.2 we found that the BHBH merger rate densities predicted from binary population synthesis are relatively sensitive to $\mathcal{S}(Z, z)$ uncertainties and might thereby present a good test bed to constrain $\mathcal{S}(Z, z)$ prescriptions. Similarly, we found that the NSNS merger rate densities might be a good test bed to constrain stellar evolution models. These findings are in agreement with, and expand on, earlier work by [Chruślińska et al. \(2019\)](#); [Neijssel et al. \(2019\)](#); [Tang et al. \(2020\)](#); [Santoliquido et al. \(2021\)](#). Simultaneously comparing the predictions for all three DCO flavors can further aid in constraining models, as shown in Figure 2 for the merger rate densities. Another example is that we showed in §3.4 that the BHNS distribution shapes might particularly be a good test bed for stellar evolution models (Figure 5), whilst the shape of the mass distributions of BHBH and NSNS detections are impacted by both stellar evolution and our $\mathcal{S}(Z, z)$ model assumptions (Figure 4). We emphasize that understanding to which uncertainty these different DCO observable properties are sensitive to also aids in understanding where to best spend computational time and work in the simulations. We showed in §3.4.2 that some population synthesis results are robust under our 560 model variations. These features are important when identifying distinguishable characteristics of the isolated binary evolution channel compared to other formation channels. Constraining and learning from population synthesis models can be further aided in the future by additional constraints including those from redshift dependent rates and redshift dependent distribution shapes (cf. [Briel et al. 2021](#); [Chu et al. 2021](#); [Santoliquido et al. 2021](#)) and additional observational constraints including those from electromagnetic observations of X-ray binaries (e.g., [Belczynski et al. 2020](#); [Vinciguerra et al. 2020](#)), Galactic pulsar binaries (e.g. [Kruckow et al. 2018](#); [Vigna-Gómez et al. 2018](#); [Chattopadhyay et al. 2020, 2021](#)), short gamma-ray bursts (e.g. [Mandhai et al. 2021](#); [Zevin et al. 2020b](#)), or GW detections beyond LVK including Cosmic Explorer and *LISA* (e.g. [Shao & Li 2018](#); [Ng et al. 2021](#); [Wagg et al. 2021](#)).

4.2 Comparison with GW mergers

At the time of writing the LVK collaboration published the latest GW catalog (GWTC-3; [The LIGO Scientific Collaboration et al. 2021b](#)) containing a total of 76 events with a false alarm rate of $\lesssim 1 \text{ yr}^{-1}$, consisting of 72 BHBH mergers, 2 NSNS mergers and 2 BHNS

events [The LIGO Scientific Collaboration et al. \(2021c\)](#)¹¹. From these detections, the LVK inferred local merger rate densities¹² of $\mathcal{R}_m^{0,\text{BHBH}} = 16\text{--}130 \text{ Gpc}^{-3} \text{ yr}^{-1}$, $\mathcal{R}_m^{0,\text{BHNS}} = 7.4\text{--}320 \text{ Gpc}^{-3} \text{ yr}^{-1}$, and $\mathcal{R}_m^{0,\text{NSNS}} = 16\text{--}1900 \text{ Gpc}^{-3} \text{ yr}^{-1}$ ([The LIGO Scientific Collaboration et al. 2021c](#)). We showed in Figure 2 that the majority of our 560 model realizations match these inferred local merger rates. However, we also found that a subset of the $\mathcal{S}(Z, z)$ models overestimate the BHBH merger rate, and that most of our models are at the lower end of the NSNS merger rate. If we scale our predicted merger ratios (Figure 3) to the 72 BHBH detections, we find a predicted range of 0–25 BHNS and 0–3 NSNS detections. Although these simulation ranges encompass the DCO numbers found in the GWTC-3 catalog, the majority of models seem to particularly underestimate the number of NSNS mergers. This is consistent with findings by other studies on isolated binary evolution populations (e.g., [Giacobbo & Mapelli 2018](#); [Chruślińska et al. 2018](#); [Santoliquido et al. 2021](#)), which indicated that matching the observed NSNS rate might require higher values for α_{CE} and/or smaller SN natal kicks. The NSNS rates could also relatively increase by changes in the mass transfer stability prescriptions (ζ) and envelope binding energy models (λ), which are not explored in our study (see [Han et al. 2020](#); [Lau et al. 2021](#), and references therein). Future observations and simulations can further constrain this.

Beyond the merger rates, GWTC-3 also provides the inferred mass distributions of the detected BHBH mergers. In Figure 10 we provide a comparison between the inferred BHBH chirp mass distribution and our set of simulations. We find that the majority of our models predict chirp mass distributions that are largely consistent with the inferred chirp mass distribution (and individual posterior distributions) for $\mathcal{M}_c \lesssim 35 M_\odot$. Figure 10 shows that particularly the SN remnant mass model variations (model L, M, N and O) significantly impact the lower and higher chirp mass end of the distributions in this comparison. On the other hand, we find that most of model realizations do not match the several detected BHBH mergers with chirp masses $\geq 35 M_\odot$. Examples include GW190521 with $\mathcal{M}_c = 69.2^{+17.0}_{-10.6} M_\odot$, GW190602 with $\mathcal{M}_c = 49.1^{+9.1}_{-8.5} M_\odot$, GW190620 with $\mathcal{M}_c = 38.3^{+8.3}_{-6.5} M_\odot$, GW190701 with $\mathcal{M}_c = 40.3^{+5.4}_{-4.9} M_\odot$ and GW190706 with $\mathcal{M}_c = 42.7^{+10.0}_{-7.0} M_\odot$, which all have at least one component with an inferred median BH mass of $m_{\text{BH},1} \gtrsim 42 M_\odot$, which is our implemented (pulsational) pair-instability SN BH mass limit. Moreover, even in model O, the model in which we assume that pair-instability SN do not occur, we find that 95% (99%) of the detectable BHBH chirp masses are expected to be below $\lesssim 50$ ($\lesssim 60$) M_\odot (Figure 4), making it challenging to explain the inferred BH mass in GW190521 and the higher mass range of the chirp mass distribution as shown in Figure 10. The origin of these massive BHs systems is still under debate. One possibility is that the location of the pair-instability mass gap could be shifted to higher masses (e.g. [Spera & Mapelli 2017](#); [Farmer et al. 2019, 2020](#); [Costa et al. 2021](#); [Mehta et al. 2021](#); [Woosley & Heger 2021](#)). Another possibility is that BHBH mergers with massive BHs formed through channels other than the isolated binary evolution channel. For example, [Tanikawa et al. \(2021\)](#) showed that formation from population III stars can account for the missing high mass BHBH mergers in isolated binary evolution studies like ours that only model population I and II stars. Other formation channels have also been suggested

¹¹ We follow the most likely classification as reported in [The LIGO Scientific Collaboration et al. \(2021c\)](#). This includes classifying GW190814 as a BHBH event.

¹² Assuming a merger rate constant in redshift.

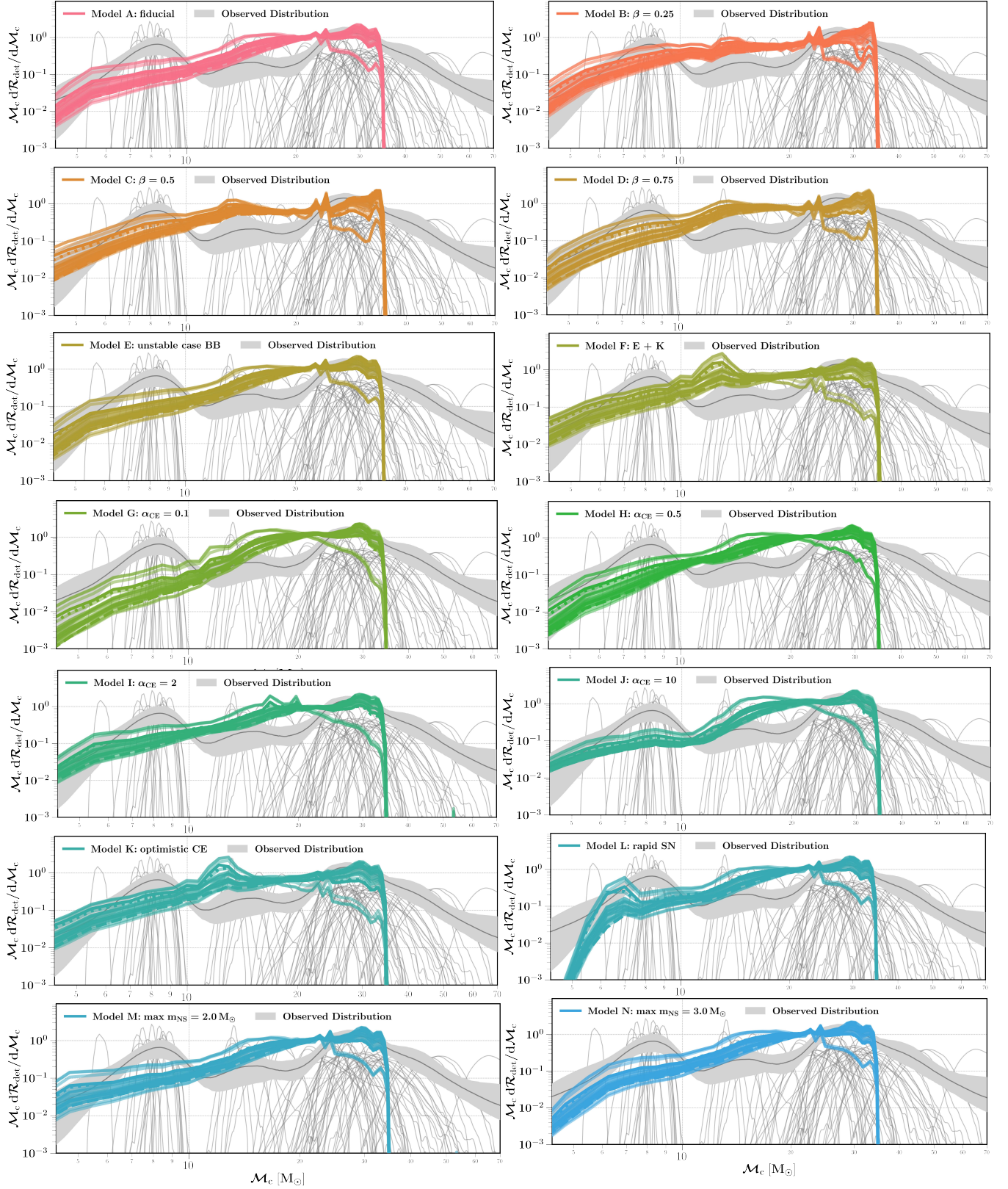


Figure 10. Differential detectable merger rate as a function of chirp mass \mathcal{M}_c $d\mathcal{R}_{\text{det}}/d\mathcal{M}_c$. Colored distributions show the expected distribution from our simulations. The gray filled distribution shows the 90% interval and median (black line) for the distribution inferred from observations, and in the background the posterior sample distributions for individual BHBH-events are shown (The LIGO Scientific Collaboration et al. 2021c, see Figure 2). All chirp mass distributions are normalized. [B](#) [E](#)

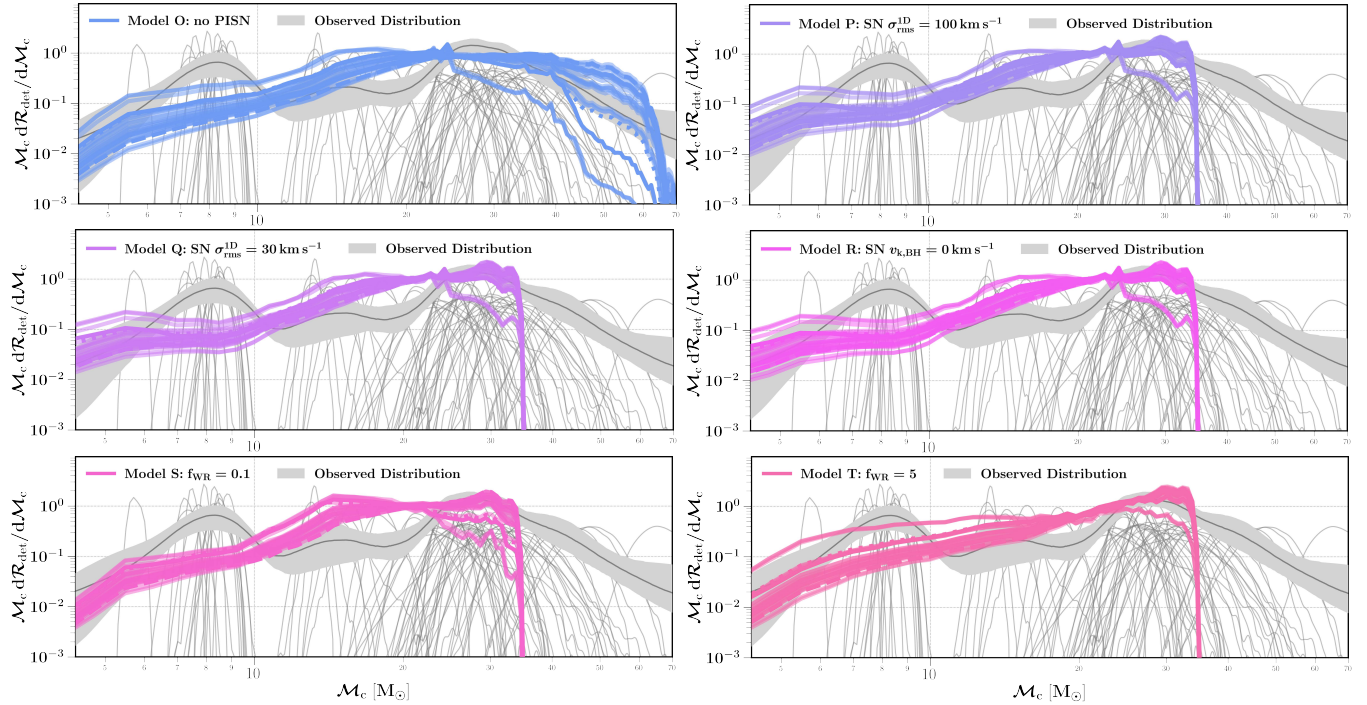


Figure 10. Continuation of Figure 10. [B](#)

for these massive BHBH mergers including hierarchical dynamical mergers (e.g. [Rodríguez et al. 2015, 2016](#); [Anagnostou et al. 2020](#)), stellar mergers (e.g. [Spera et al. 2019](#); [Di Carlo et al. 2020](#); [Kremer et al. 2020](#)), triples (e.g. [Vigna-Gómez et al. 2021](#)) or mergers in AGN disks (e.g. [Secunda et al. 2020](#)). For a more detailed discussion see, for example, [Abbott et al. \(2020e\)](#) and [Kimball et al. \(2021\)](#) and references therein. Future studies should explore a full comparison with LVK data to further constrain models.

5 CONCLUSIONS

In this study we simulated the rates and properties of BHBH, BHNS and NSNS mergers detectable with existing GW detectors. We simultaneously examined the impact of two key modelling uncertainties in population synthesis studies: uncertainties arising from massive binary star evolution, and from the metallicity-dependent star formation history, $S(Z, z)$. We accomplish this by simulating populations of binaries over a grid of 53 birth metallicity values and taking into account the $S(Z, z)$ and GW detection probability. The resulting suite of 560 model realizations (20 binary stellar evolution variations \times 28 $S(Z, z)$ variations) is the largest of its kind, and made publicly available. Our main findings within the context of the variations we considered are summarized below.

- **Merging DCO formation yields:** We find for all our stellar evolution variations that the merging BHBH (BHNS) formation yield is typically a rapidly decreasing function of metallicity at $Z \gtrsim Z_{\odot}/10$ ($\gtrsim Z_{\odot}/2$) as a result of line-driven Wolf-Rayet like winds. The NSNS yield, on the other hand, is relatively independent of metallicity. We find that the formation yield of BHBH mergers for $Z \lesssim Z_{\odot}/10$ is remarkably constant over massive binary-star models and Z . The formation yields of BHNS and NSNS mergers are impacted over the full metallicity range by our massive binary-star

assumptions (see Figure 1).

- **Merging DCO rates:** We find that the calculated intrinsic and detectable merger rate densities (\mathcal{R}_m^0 and \mathcal{R}_{det} , respectively) can be impacted by factors $\approx 210 \times -1300 \times$ due to combined uncertainties in stellar evolution and $S(Z, z)$. The 560 model variations lead to estimated merger rate densities in the ranges $\mathcal{R}_m^{0, \text{BHBH}} = 3.8 - 810 \text{ Gpc}^{-3} \text{ yr}^{-1}$ and $\mathcal{R}_{\text{det}}^{\text{BHBH}} = 17 - 12000 \text{ yr}^{-1}$ for BHBHs, $\mathcal{R}_m^{0, \text{BHNS}} = 2.2 - 830 \text{ Gpc}^{-3} \text{ yr}^{-1}$ and $\mathcal{R}_{\text{det}}^{\text{BHNS}} = 0.36 - 180 \text{ yr}^{-1}$ for BHNSs, and $\mathcal{R}_m^{0, \text{NSNS}} = 0.32 - 330 \text{ Gpc}^{-3} \text{ yr}^{-1}$ and $\mathcal{R}_{\text{det}}^{\text{NSNS}} = 0 - 12 \text{ yr}^{-1}$ for NSNSs, for a ground-based GW detector consisting of LIGO-Virgo-KAGRA at design sensitivity. In particular, we found that the estimated BHBH merger rate densities are relatively sensitive to our explored $S(Z, z)$ uncertainties and might thereby present a good test bed to constrain $S(Z, z)$ prescriptions. On the other hand, we found that the NSNS merger rate densities are sensitive to stellar evolution models and therefore might be a good test bed to constrain stellar evolution models. For BHNSs we find that the calculated rates are significantly impacted by both uncertainties (see Figures 2 and 3).

- **Merging DCO mass distribution shapes:** We show in Figures 4, 5 and 6 the impact from the massive binary-star and $S(Z, z)$ variations on the (normalized) shape of the detectable DCO mass distributions (chirp mass, individual component masses and mass ratios). We find that the shape of the BHNS mass distributions are dominated by variations in binary stellar evolution within our model explorations. For BHBH and NSNS mergers we find that the mass distribution shapes are impacted by both variations in stellar evolution and $S(Z, z)$.

- **Merging DCO t_{delay} and Z distribution shapes:** We show in Figures 7, 8 and 9 the impact from binary stellar evolution and $S(Z, z)$ variations on the delay time and birth metallicity

distributions calculated in our models. We find that the $S(Z, z)$ has a significant impact for BHBH, BHNS and NSNS on the shape of the delay time and metallicity distributions of detectable mergers. Several stellar evolution models, including those affecting stellar winds, can also significantly impact the delay time and Z distribution shapes.

- **Consistent features among our 560 model variations:** We find several features in the DCO mass distributions that are consistent among all our 560 model variations. First, we find that at least 95% (99%) of the detectable BHBH mergers have mass ratios $q \lesssim 4$ ($q \lesssim 6$) in all 560 model variations (fifth column Figure 4). Second, we find that more than 95% of BHBH mergers are always expected to contain a BH with a mass $\gtrsim 8 M_{\odot}$ (third column Figure 4). Third, we find that less than 5% of the detectable merging BHNS systems have BH masses $m_{\text{BH}} \gtrsim 18 M_{\odot}$ (third column Figure 5). Fourth we find that NSs in NSNS mergers are expected to have lower masses on average compared to NSs in BHNS mergers (Figures 5 and 6). We discuss how these findings are marginally consistent with GW observations from GWTC-3 in §3.4.2 and §4.2.


Overall, our results highlight the importance of considering the uncertainty in both the stellar evolution and metallicity-dependent star formation history when exploring population synthesis simulations of BHNS, BHBH and NSNS mergers and when trying to infer model properties from GW data.

ACKNOWLEDGEMENTS

The authors thank everyone in the COMPAS collaboration and Berger Time-Domain Group for help. In addition, the authors thank the Harvard FAS research computing group for technical support on the simulations and high performance computing part of the research. The authors also thank Shanika Galaudage and Victoria DiTomasso for their help with this paper. FSB thanks Christopher Brown and Katie Callam for organizing the ‘writing oasis’. Lastly, FSB wants to acknowledge the amount of serendipity and privilege that was involved to end up pursuing this astronomy research. The Berger Time-Domain Group is supported in part by NSF and NASA grants. Some of the authors are supported by the Australian Research Council Centre of Excellence for Gravitational Wave Discovery (OzGrav), through project number CE170100004. FSB is supported in part by the Prins Bernard Cultuurfonds studiebeurs 2021. IM is a recipient of the Australian Research Council Future Fellowship FT190100574. A.V-G. acknowledges funding support by the Danish National Research Foundation (DNRF132). SJ, LvS and SdM acknowledge funding from the Netherlands Organisation for Scientific Research (NWO), as part of the Vidi research program BinWaves (project number 639.042.728) and the European Union’s Horizon 2020 research and innovation program from the European Research Council (ERC, Grant agreement No. 715063). LvS, TW and SdM acknowledge support by the National Science Foundation under Grant No. (NSF 2009131). This research has made use of NASA’s Astrophysics Data System Bibliographic Services. This research has made use of data, software and/or web tools obtained from the Gravitational Wave Open Science Center (<https://www.gw-openscience.org/>), a service of LIGO Laboratory, the LIGO Scientific Collaboration and the Virgo Collaboration. LIGO Laboratory and Advanced LIGO (LIGO Scientific Collaboration et al. 2015) are funded by the United States National Science Foundation (NSF) as well as the Science and Technology Facilities Council (STFC) of the United Kingdom, the Max-Planck-Society (MPS), and the State of Niedersachsen/Germany for support

of the construction of Advanced LIGO and construction and operation of the GEO600 detector. Additional support for Advanced LIGO was provided by the Australian Research Council. Virgo (Acernese et al. 2015) is funded, through the European Gravitational Observatory (EGO), by the French Centre National de Recherche Scientifique (CNRS), the Italian Istituto Nazionale di Fisica Nucleare (INFN) and the Dutch Nikhef, with contributions by institutions from Belgium, Germany, Greece, Hungary, Ireland, Japan, Monaco, Poland, Portugal, Spain (The LIGO Scientific Collaboration et al. 2021a).

DATA AVAILABILITY

All data used in this work is publicly available on Zenodo at Broekgaarden (2021a, BHBH) Broekgaarden (2021b, BHNS) and Broekgaarden (2021c, NSNS). All code to reproduce the results and figures in this paper (and additional figures) are publicly available on Github at <https://github.com/FloorBroekgaarden/Double-Compact-Object-Mergers> .

SOFTWARE

Simulations in this paper made use of the COMPAS rapid binary population synthesis code, which is freely available at <http://github.com/TeamCOMPAS/COMPAS> (Team COMPAS: J. Riley et al. 2021) including work based on (Stevenson et al. 2017; Barrett et al. 2018; Vigna-Gómez et al. 2018; Broekgaarden et al. 2019). The simulations performed in this work were simulated with a COMPAS version that predates the publicly available code. Our version of the code is most similar to version 02.13.01 of the publicly available COMPAS code. Requests for the original code can be made to the lead author. The authors used STROOPWAFEL from (Broekgaarden et al. 2019), publicly available at <https://github.com/FloorBroekgaarden/STROOPWAFEL>¹³.

The authors made use of PYTHON from the Python Software Foundation. Python Language Reference, version 3.6. Available at <http://www.python.org> (van Rossum 1995). In addition the following Python packages were used: MATPLOTLIB (Hunter 2007), NUMPY (Harris et al. 2020), SCIPLY (Virtanen et al. 2020), IPYTHON/JUPYTER (Perez & Granger 2007; Kluyver et al. 2016), PANDAS (Wes McKinney 2010), SEABORN (Waskom & the seaborn development team 2020), ASTROPY (Astropy Collaboration et al. 2018) and HDF5 (Collette 2013).

Figure 10 makes use of the MAKE_PLOTS_VAMANA.PY code by Vaibhav Tiwari on behalf of the LIGO Scientific Collaboration, Virgo Collaboration and KAGRA Collaboration provided under the Creative Commons Attribution 4.0 licence. We obtained their code from Zenodo doi:10.5281/zenodo.5655785, which makes use of the kernel density estimator as provided in <https://dcc.ligo.org/LIGO-T2100447/public> (Sadiq et al. 2021). The simulations were performed on the super computers from the Harvard FAS research computing group.

REFERENCES

Abbott B. P., et al., 2017, *Phys. Rev. Lett.*, 119, 161101

¹³ For the latest pip installable version of STROOPWAFEL please contact the corresponding author.

- Abbott B. P., et al., 2019, *Physical Review X*, **9**, 031040
- Abbott B. P., Abbott R., Abbott T. D., others Zweizig J., 2020a, *Living Reviews in Relativity*, **23**, 3
- Abbott R., et al., 2020b, *Phys. Rev. D*, **102**, 043015
- Abbott B. P., et al., 2020c, *ApJ*, **892**, L3
- Abbott R., et al., 2020d, *ApJ*, **896**, L44
- Abbott R., et al., 2020e, *ApJ*, **900**, L13
- Abbott R., et al., 2021a, *Physical Review X*, **11**, 021053
- Abbott R., et al., 2021b, *ApJ*, **913**, L7
- Abbott R., et al., 2021c, *ApJ*, **915**, L5
- Acernese F., et al., 2015, *Classical and Quantum Gravity*, **32**, 024001
- Agrawal P., Hurley J., Stevenson S., Szécsi D., Flynn C., 2020, *MNRAS*, **497**, 4549
- Anagnostou O., Trenti M., Melatos A., 2020, arXiv e-prints, p. [arXiv:2010.06161](https://arxiv.org/abs/2010.06161)
- Arca Sedda M., 2021, *ApJ*, **908**, L38
- Astropy Collaboration et al., 2018, *AJ*, **156**, 123
- Barrett J. W., Gaebel S. M., Neijssel C. J., Vigna-Gómez A., Stevenson S., Berry C. P. L., Farr W. M., Mandel I., 2018, *MNRAS*, **477**, 4685
- Bavera S. S., et al., 2021, *A&A*, **647**, A153
- Belczynski K., Kalogera V., Rasio F. A., Taam R. E., Zezas A., Bulik T., Maccarone T. J., Ivanova N., 2008, *ApJS*, **174**, 223
- Belczynski K., Dominik M., Bulik T., O’Shaughnessy R., Fryer C., Holz D. E., 2010, *ApJ*, **715**, L138
- Belczynski K., et al., 2020, *A&A*, **636**, A104
- Belczynski K., et al., 2021, arXiv e-prints, p. [arXiv:2108.10885](https://arxiv.org/abs/2108.10885)
- Bhattacharya D., van den Heuvel E. P. J., 1991, *Phys. Rep.*, **203**, 1
- Boco L., Lapi A., Chruslinska M., Donevski D., Sicilia A., Danese L., 2021, *ApJ*, **907**, 110
- Bouffanais Y., Mapelli M., Gerosa D., Di Carlo U. N., Giacobbo N., Berti E., Baibhav V., 2019, *ApJ*, **886**, 25
- Bouffanais Y., Mapelli M., Santoliquido F., Giacobbo N., Di Carlo U. N., Rastello S., Artale M. C., Iorio G., 2021, *MNRAS*, **507**, 5224
- Briel M. M., Eldridge J. J., Stanway E. R., Stevance H. F., Chrimes A. A., 2021, arXiv e-prints, p. [arXiv:2111.08124](https://arxiv.org/abs/2111.08124)
- Broekgaarden F. S., 2021a, BHBH simulations from: Impact of Massive Binary Star and Cosmic Evolution on Gravitational Wave Observations II: Double Compact Object Mergers, [doi:10.5281/zenodo.5651073](https://doi.org/10.5281/zenodo.5651073), <https://doi.org/10.5281/zenodo.5651073>
- Broekgaarden F. S., 2021b, BHNS simulations from: Impact of Massive Binary Star and Cosmic Evolution on Gravitational Wave Observations II: Double Compact Object Mergers, [doi:10.5281/zenodo.5178777](https://doi.org/10.5281/zenodo.5178777), <https://doi.org/10.5281/zenodo.5178777>
- Broekgaarden F. S., 2021c, NSNS simulations from: Impact of Massive Binary Star and Cosmic Evolution on Gravitational Wave Observations II: Double Compact Object Mergers, [doi:10.5281/zenodo.5189849](https://doi.org/10.5281/zenodo.5189849), <https://doi.org/10.5281/zenodo.5189849>
- Broekgaarden F. S., Berger E., 2021, *ApJ*, **920**, L13
- Broekgaarden F. S., et al., 2019, *MNRAS*, **490**, 5228
- Broekgaarden F. S., et al., 2021, *MNRAS*,
- Chattopadhyay D., Stevenson S., Hurley J. R., Rossi L. J., Flynn C., 2020, *MNRAS*, **494**, 1587
- Chattopadhyay D., Stevenson S., Hurley J. R., Bailes M., Broekgaarden F., 2021, *MNRAS*, **504**, 3682
- Chruslinska M., Nelemans G., 2019, *MNRAS*, **488**, 5300
- Chruslinska M., Belczynski K., Kléncki J., Benacquista M., 2018, *MNRAS*, **474**, 2937
- Chruslinska M., Nelemans G., Belczynski K., 2019, *MNRAS*, **482**, 5012
- Chruslinska M., Nelemans G., Boco L., Lapi A., 2021, *MNRAS*,
- Chu Q., Yu S., Lu Y., 2021, *MNRAS*,
- Collette A., 2013, Python and HDF5. O’Reilly
- Costa G., Bressan A., Mapelli M., Marigo P., Iorio G., Spera M., 2021, *MNRAS*, **501**, 4514
- Dabrowsny M., Giacobbo N., Gerosa D., 2021, *Rendiconti Lincei. Scienze Fisiche e Naturali*,
- de Kool M., 1990, *ApJ*, **358**, 189
- de Mink S. E., Belczynski K., 2015, *ApJ*, **814**, 58
- de Mink S. E., Mandel I., 2016, *MNRAS*, **460**, 3545
- Delgado A. J., Thomas H. C., 1981, *A&A*, **96**, 142
- Dewi J. D. M., Pols O. R., 2003, *MNRAS*, **344**, 629
- Di Carlo U. N., Mapelli M., Bouffanais Y., Giacobbo N., Santoliquido F., Bressan A., Spera M., Haardt F., 2020, *MNRAS*, **497**, 1043
- Dominik M., Belczynski K., Fryer C., Holz D. E., Berti E., Bulik T., Mandel I., O’Shaughnessy R., 2012, *ApJ*, **759**, 52
- Dominik M., et al., 2015, *ApJ*, **806**, 263
- du Buisson L., et al., 2020, *MNRAS*, **499**, 5941
- Farmer R., Renzo M., de Mink S. E., Marchant P., Justham S., 2019, *ApJ*, **887**, 53
- Farmer R., Renzo M., de Mink S. E., Fishbach M., Justham S., 2020, *ApJ*, **902**, L36
- Fishbach M., Kalogera V., 2021, *ApJ*, **914**, L30
- Fragione G., 2021, arXiv e-prints, p. [arXiv:2110.09604](https://arxiv.org/abs/2110.09604)
- Franciolini G., et al., 2021, arXiv e-prints, p. [arXiv:2105.03349](https://arxiv.org/abs/2105.03349)
- Fryer C. L., Belczynski K., Wiktorowicz G., Dominik M., Kalogera V., Holz D. E., 2012, *ApJ*, **749**, 91
- Furlong M., et al., 2015, *MNRAS*, **450**, 4486
- Giacobbo N., Mapelli M., 2018, *MNRAS*, **480**, 2011
- Giacobbo N., Mapelli M., Spera M., 2018, *MNRAS*, **474**, 2959
- Hamann W. R., Koesterke L., 1998, *A&A*, **335**, 1003
- Hamann W. R., et al., 2019, *A&A*, **625**, A57
- Han Z.-W., Ge H.-W., Chen X.-F., Chen H.-L., 2020, *Research in Astronomy and Astrophysics*, **20**, 161
- Harris C. R., et al., 2020, *Nature*, **585**, 357–362
- Hinshaw G., et al., 2013, *ApJS*, **208**, 19
- Hunter J. D., 2007, *Computing in Science and Engineering*, **9**, 90
- Hurley J. R., Pols O. R., Tout C. A., 2000, *MNRAS*, **315**, 543
- Hurley J. R., Tout C. A., Pols O. R., 2002, *MNRAS*, **329**, 897
- Im M., et al., 2017, *ApJ*, **849**, L16
- Ivanova N., Justham S., Ricker P., 2020, Common Envelope Evolution, [doi:10.1088/2514-3433/abb6f0](https://doi.org/10.1088/2514-3433/abb6f0).
- Kalogera V., Webbink R. F., 1996, *ApJ*, **458**, 301
- Kimball C., et al., 2021, *ApJ*, **915**, L35
- Kléncki J., Moe M., Gladysz W., Chruslinska M., Holz D. E., Belczynski K., 2018, *A&A*, **619**, A77
- Kléncki J., Nelemans G., Istrate A. G., Chruslinska M., 2021, *A&A*, **645**, A54
- Kluyver T., et al., 2016, in *ELPUB*. pp 87–90
- Kremer K., et al., 2020, *ApJ*, **903**, 45
- Kruckow M. U., Tauris T. M., Langer N., Kramer M., Izzard R. G., 2018, *MNRAS*, **481**, 1908
- LIGO Scientific Collaboration et al., 2015, *Classical and Quantum Gravity*, **32**, 074001
- Lamberts A., Garrison-Kimmel S., Clausen D. R., Hopkins P. F., 2016, *MNRAS*, **463**, L31
- Langer N., Norman C. A., 2006, *ApJ*, **638**, L63
- Laplace E., Göteborg Y., de Mink S. E., Justham S., Farmer R., 2020, *A&A*, **637**, A6
- Lau M. Y. M., Hirai R., González-Bolívar M., Price D. J., De Marco O., Mandel I., 2021, arXiv e-prints, p. [arXiv:2111.00923](https://arxiv.org/abs/2111.00923)
- Linden T., Kalogera V., Sepinsky J. F., Prestwich A., Zezas A., Gallagher J. S., 2010, *ApJ*, **725**, 1984
- Lu W., Beniamini P., Bonnerot C., 2021, *MNRAS*, **500**, 1817
- Ma X., Hopkins P. F., Faucher-Giguère C.-A., Zolman N., Muratov A. L., Kereš D., Quataert E., 2016, *MNRAS*, **456**, 2140
- Madau P., Dickinson M., 2014, *ARA&A*, **52**, 415
- Madau P., Fragos T., 2017, *ApJ*, **840**, 39
- Mandel I., Broekgaarden F. S., 2021, arXiv e-prints, p. [arXiv:2107.14239](https://arxiv.org/abs/2107.14239)
- Mandel I., Farmer A., 2018, arXiv e-prints, p. [arXiv:1806.05820](https://arxiv.org/abs/1806.05820)
- Mandel I., Müller B., Riley J., de Mink S. E., Vigna-Gómez A., Chattopadhyay D., 2021, *MNRAS*, **500**, 1380
- Mandhai S., Lamb G. P., Tanvir N. R., Bray J., Nixon C. J., Eyles-Ferris R. A. J., Levan A. J., Gompertz B. P., 2021, arXiv e-prints, p. [arXiv:2109.09714](https://arxiv.org/abs/2109.09714)
- Mapelli M., 2021, Formation Channels of Single and Binary Stellar-Mass Black Holes. p. 4, [doi:10.1007/978-981-15-4702-7_16-1](https://doi.org/10.1007/978-981-15-4702-7_16-1)
- Mapelli M., Giacobbo N., Ripamonti E., Spera M., 2017, *MNRAS*, **472**, 2422

- Mapelli M., Spera M., Montanari E., Limongi M., Chieffi A., Giacobbo N., Bressan A., Bouffanais Y., 2020, *ApJ*, **888**, 76
- Marchant P., Langer N., Podsiadlowski P., Tauris T. M., de Mink S., Mandel I., Moriya T. J., 2017, *A&A*, **604**, A55
- Marchant P., Renzo M., Farmer R., Pappas K. M. W., Taam R. E., de Mink S. E., Kalogera V., 2019, *ApJ*, **882**, 36
- Marchant P., Pappas K. M. W., Gallegos-Garcia M., Berry C. P. L., Taam R. E., Kalogera V., Podsiadlowski P., 2021, *A&A*, **650**, A107
- Massevitch A., Yungelson L., 1975, *Mem. Soc. Astron. Italiana*, **46**, 217
- McKernan B., Ford K. E. S., O’Shaughnessy R., 2020, *MNRAS*, **498**, 4088
- Mehta A. K., Buonanno A., Gair J., Miller M. C., Farag E., deBoer R. J., Wiescher M., Timmes F. X., 2021, arXiv e-prints, p. [arXiv:2105.06366](https://arxiv.org/abs/2105.06366)
- Moe M., Di Stefano R., 2017, *The Astrophysical Journal Supplement Series*, **230**, 15
- Neijssel C. J., et al., 2019, *MNRAS*, **490**, 3740
- Ng K. K. Y., Vitale S., Farr W. M., Rodriguez C. L., 2021, *ApJ*, **913**, L5
- Olejak A., Belczynski K., Ivanova N., 2021, *A&A*, **651**, A100
- Paczynski B., Sienkiewicz R., 1972, *Acta Astron.*, **22**, 73
- Panther B., Heavens A. F., Jimenez R., 2004, *MNRAS*, **355**, 764
- Perez F., Granger B. E., 2007, *Computing in Science and Engineering*, **9**, 21
- Pfahl E., Rappaport S., Podsiadlowski P., 2002, *ApJ*, **571**, L37
- Podsiadlowski P., Langer N., Poelarends A. J. T., Rappaport S., Heger A., Pfahl E., 2004, *ApJ*, **612**, 1044
- Rastello S., Mapelli M., Di Carlo U. N., Giacobbo N., Santoliquido F., Spera M., Ballone A., Iorio G., 2020, *MNRAS*, **497**, 1563
- Renzo M., et al., 2019, *A&A*, **624**, A66
- Rodriguez C. L., Morscher M., Pattabiraman B., Chatterjee S., Haster C.-J., Rasio F. A., 2015, *Phys. Rev. Lett.*, **115**, 051101
- Rodriguez C. L., Chatterjee S., Rasio F. A., 2016, *Phys. Rev. D*, **93**, 084029
- Román-Garza J., et al., 2021, *ApJ*, **912**, L23
- Sadiq J., Dent T., Wysocki D., 2021, Available as LIGO-T2100447
- Safarzadeh M., Berger E., Ng K. K. Y., Chen H.-Y., Vitale S., Whittle C., Scannapieco E., 2019, *ApJ*, **878**, L13
- Sana H., 2017, in Eldridge J. J., Bray J. C., McClelland L. A. S., Xiao L., eds, *IAU Symposium Vol. 329, The Lives and Death-Throes of Massive Stars*. pp 110–117 ([arXiv:1703.01608](https://arxiv.org/abs/1703.01608)), doi:10.1017/S1743921317003209
- Sander A. A. C., Vink J. S., 2020, *MNRAS*, **499**, 873
- Santoliquido F., Mapelli M., Giacobbo N., Bouffanais Y., Artale M. C., 2021, *MNRAS*, **502**, 4877
- Schneider F. R. N., Izzard R. G., Langer N., de Mink S. E., 2015, *ApJ*, **805**, 20
- Schootemeijer A., Langer N., Grin N. J., Wang C., 2019, *A&A*, **625**, A132
- Secunda A., et al., 2020, *ApJ*, **903**, 133
- Shao Y., Li X.-D., 2018, *ApJ*, **867**, 124
- Shenar T., et al., 2019, *A&A*, **627**, A151
- Smarr L. L., Blandford R., 1976, *ApJ*, **207**, 574
- Soberman G. E., Phinney E. S., van den Heuvel E. P. J., 1997, *A&A*, **327**, 620
- Spera M., Mapelli M., 2017, *MNRAS*, **470**, 4739
- Spera M., Mapelli M., Giacobbo N., Trani A. A., Bressan A., Costa G., 2019, *MNRAS*, **485**, 889
- Srinivasan G., 1989, *A&ARv*, **1**, 209
- Stevenson S., Vigna-Gómez A., Mandel I., Barrett J. W., Neijssel C. J., Perkins D., de Mink S. E., 2017, *Nature Communications*, **8**, 14906
- Stevenson S., Sampson M., Powell J., Vigna-Gómez A., Neijssel C. J., Szécsi D., Mandel I., 2019, *ApJ*, **882**, 121
- Strolger L.-G., et al., 2004, *ApJ*, **613**, 200
- Tang P. N., Eldridge J. J., Stanway E. R., Bray J. C., 2020, *MNRAS*, **493**, L6
- Tanikawa A., Yoshida T., Kinugawa T., Trani A. A., Hosokawa T., Susa H., Omukai K., 2021, arXiv e-prints, p. [arXiv:2110.10846](https://arxiv.org/abs/2110.10846)
- Tauris T. M., et al., 2017, *ApJ*, **846**, 170
- Team COMPAS: J. Riley et al., 2021, arXiv e-prints, p. [arXiv:2109.10352](https://arxiv.org/abs/2109.10352)
- The LIGO Scientific Collaboration the Virgo Collaboration the KAGRA Collaboration 2021a, The population of merging compact binaries inferred from gravitational waves through GWTC-3 - Data release, doi:10.5281/zenodo.5655785, <https://doi.org/10.5281/zenodo.5655785>
- The LIGO Scientific Collaboration et al., 2021b, arXiv e-prints, p. [arXiv:2111.03606](https://arxiv.org/abs/2111.03606)
- The LIGO Scientific Collaboration et al., 2021c, arXiv e-prints, p. [arXiv:2111.03634](https://arxiv.org/abs/2111.03634)
- Timmes F. X., Woosley S. E., Weaver T. A., 1996, *ApJ*, **457**, 834
- van Rossum G., 1995, Technical Report CS-R9526, Python tutorial. Centrum voor Wiskunde en Informatica (CWI), Amsterdam
- van Son L. A. C., et al., 2021, arXiv e-prints, p. [arXiv:2110.01634](https://arxiv.org/abs/2110.01634)
- Vigna-Gómez A., et al., 2018, *MNRAS*, **481**, 4009
- Vigna-Gómez A., Toonen S., Ramirez-Ruiz E., Leigh N. W. C., Riley J., Haster C.-J., 2021, *ApJ*, **907**, L19
- Vinciguerra S., et al., 2020, *MNRAS*, **498**, 4705
- Vink J. S., 2017, *A&A*, **607**, L8
- Vink J. S., de Koter A., 2005, *A&A*, **442**, 587
- Virtanen P., et al., 2020, *Nature Methods*, **17**, 261
- Wagg T., Broekgaarden F. S., de Mink S. E., van Son L. A. C., Frankel N., Justham S., 2021, arXiv e-prints, p. [arXiv:2111.13704](https://arxiv.org/abs/2111.13704)
- Waskom M., the seaborn development team 2020, *mwaskom/seaborn*, doi:10.5281/zenodo.592845, <https://doi.org/10.5281/zenodo.592845>
- Webbink R. F., 1984, *ApJ*, **277**, 355
- Wes McKinney 2010, in Stéfan van der Walt Jarrod Millman eds, *Proceedings of the 9th Python in Science Conference*. pp 56 – 61, doi:10.25080/Majora-92bf1922-00a
- Woosley S. E., 2017, *ApJ*, **836**, 244
- Woosley S. E., Heger A., 2021, *ApJ*, **912**, L31
- Xu X.-J., Li X.-D., 2010a, *ApJ*, **716**, 114
- Xu X.-J., Li X.-D., 2010b, *ApJ*, **722**, 1985
- Zevin M., Pankow C., Rodriguez C. L., Sampson L., Chase E., Kalogera V., Rasio F. A., 2017, *ApJ*, **846**, 82
- Zevin M., Spera M., Berry C. P. L., Kalogera V., 2020a, *ApJ*, **899**, L1
- Zevin M., Kelley L. Z., Nugent A., Fong W.-f., Berry C. P. L., Kalogera V., 2020b, *ApJ*, **904**, 190
- Zevin M., et al., 2021, *ApJ*, **910**, 152

APPENDIX A: ADDITIONAL TABLES AND FIGURES

In this appendix we show a Table and three additional figures that are mentioned throughout the main text.

First, Table A1 summarizes the 28 $\mathcal{S}(Z, z)$ models that are explored in this study. More details about the assumptions in each model can be found in Broekgaarden et al. (2021) and Neijssel et al. (2019).

Second, in Figure A1 we show similar to Figure 1 the formation yield of DCO systems that merge in a Hubble time as a function of the birth metallicity. However, in this figure we show the relative formation yields between BHNS to BHBH (left panel) and between NSNS and BHBH (right panel). It can be seen that in most models the formation yield of BHNS mergers exceeds that of BHBH around birth metallicities $Z \gtrsim Z/2$. The yield of NSNS mergers surpasses the BHBH yield for most models around Z/Z_{\odot} .

Third, in Figure A2 we visualize two of our $\mathcal{S}(Z, z)$ model variations, $xyz = 312$ and $xyz = 231$. The $xyz = 312$ ($xyz = 231$) model is the $\mathcal{S}(Z, z)$ distribution that correspond to one of the highest (lowest) average Z and results in one of the lowest (highest) BHBH merger rates in Figure 2.

Last, Figure A3 shows a zoom in on one of the percentile distribution panels from Figure 4 (the top row, second column panel). We highlight in this figure the labels of the $\mathcal{S}(Z, z)$ models that correspond to the order of the horizontal percentile bars.

This paper has been typeset from a $\text{\TeX}/\text{\LaTeX}$ file prepared by the author.

xyz index	SFRD [x]	GSMF [y]	MZR [z]
000	preferred phenomenological model from Neijssel et al. (2019)		
1	Madau & Dickinson (2014)	Panter et al. (2004)	Langer & Norman (2006)
2	Strolger et al. (2004)	Furlong et al. (2015) single Schechter	Langer & Norman (2006) + offset
3	Madau & Fragos (2017)	Furlong et al. (2015) double Schechter	Ma et al. (2016)

Table A1. List of the assumptions for the metallicity-specific star formation rate, $S(Z, z)$, models that we explore in this study. 27 $S(Z, z)$ models are obtained by combining a star formation rate density (SFRD) with a galaxy stellar mass function (GSMF) and mass-metallicity relation (MZR). See §2.2 and paper I for more details. The models are named in the convention xyz, where x, y, z \in [1, 2, 3] are the index numbers for the models used for the SFRD, GSMF and MZR, respectively. For example, the combination of using the [Madau & Dickinson \(2014\)](#) SFRD with the [Panter et al. \(2004\)](#) GSMF and the [Ma et al. \(2016\)](#) MZR is labeled 113. The preferred phenomenological model from [Neijssel et al. \(2019\)](#) has the label 000 and is not a specific combination but a parameterized model that is built to be flexible and is fitted to match the observed BHBH merger rate and chirp mass distribution from the first two runs of LIGO and Virgo.

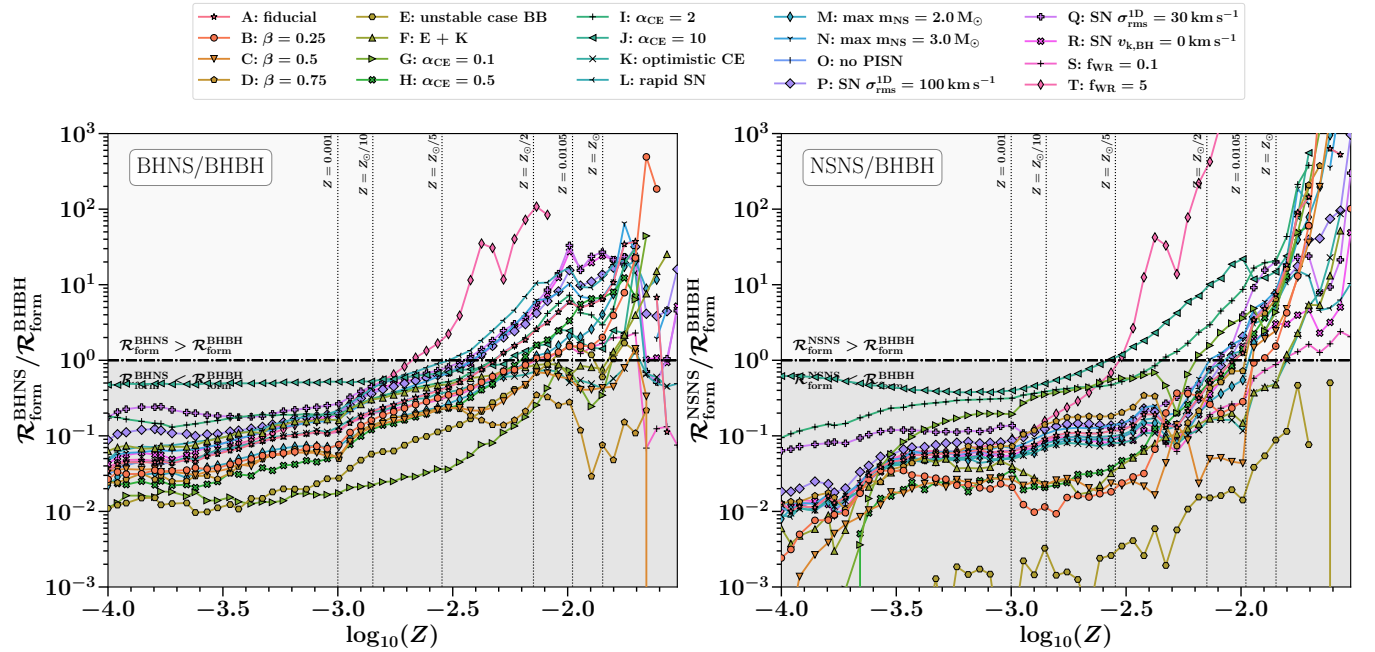


Figure A1. The ratio of formation yields of merging double compact objects per solar mass of star formation ($dN_{\text{form}}/dM_{\text{SFR}}$) as a function of birth metallicity (Z). The left panel shows the ratio of BHNS to BHBH formation yields and the right panel shows the ratio of NSNS to BHBH formation yields. Each color and marker type corresponds to one of the 20 binary population synthesis models explored in this study (Table 1). Vertical dotted lines show fixed Z values. The marker points show the Z grid points that we simulated with COMPAS. Scatter points are missing where we divide by zero. [b](#) [e](#)

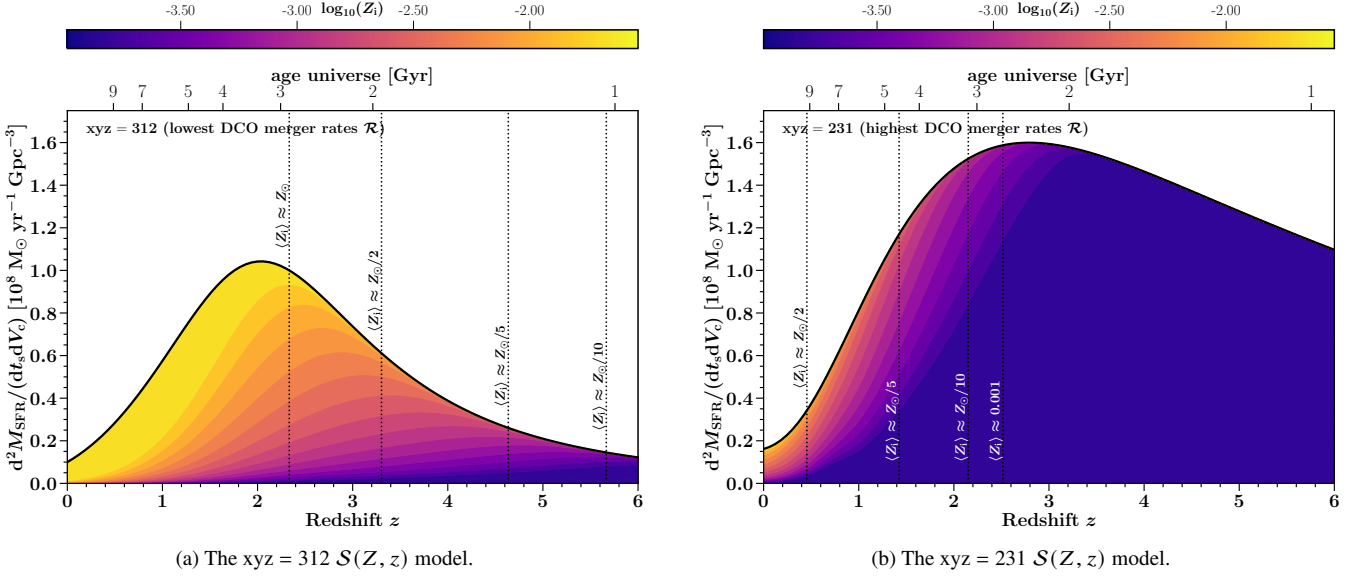


Figure A2. The SFRD as a function of redshift and metallicity for two $S(Z, z)$ models from Table A1 used in this study. The left panel shows the $xyz = 312$ $S(Z, z)$ model whilst the right panel shows the $xyz = 231$ $S(Z, z)$ model, these correspond to the $S(Z, z)$ models with the highest and lowest average Z , respectively. In color we show the build up of the SFRD from the contribution by different Z , where for visual purposes we divided the SFRD into a few metallicity bins. [📄](#) [📄](#) [📄](#)

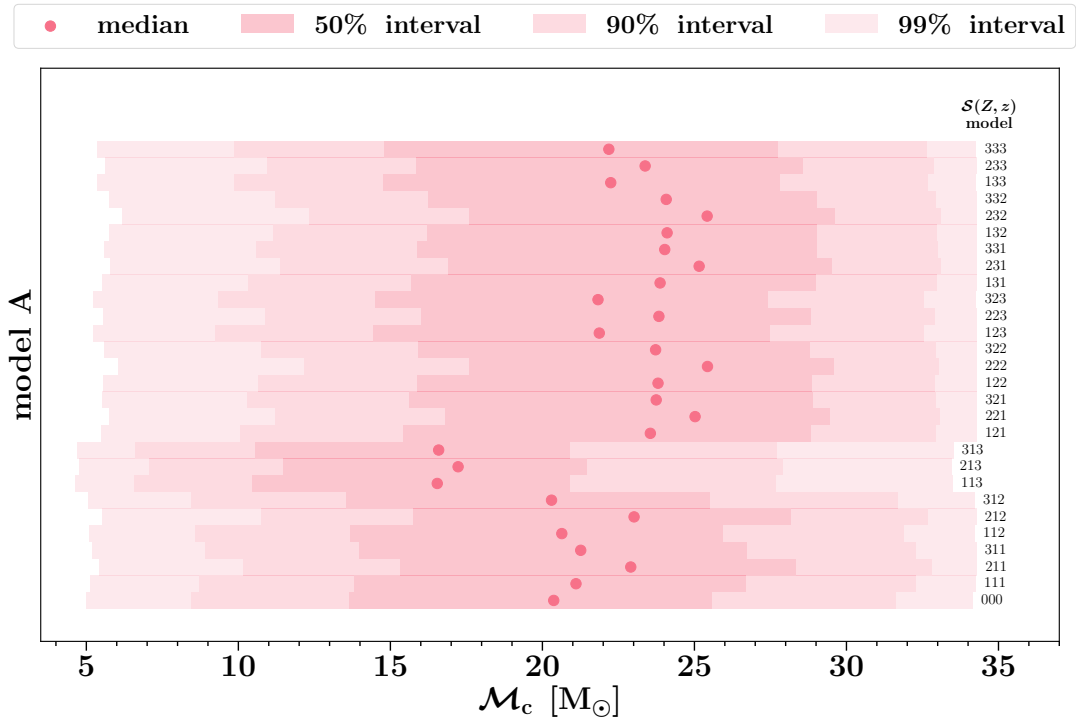


Figure A3. Zoom in on the chirp mass percentile panel for model A for detectable BHBH mergers at design sensitivity from Figure 4. Each of the 28 individual horizontal bars visualizes the median (scatter points), 50, 90 and 99 (three shades) distribution intervals. On the right of the horizontal bar we show the $S(Z, z)$ model name as given in Table A1. [📄](#) [📄](#)